5-4-2021

Photoionization and Structure of the Superheavy Atoms No, Cn and Og

Ahmad Kafaee Razavi

PHOTOIONIZATION AND STRUCTURE OF THE SUPERHEAVY ATOMS No, Cn AND Og

by

AHMAD KAFAEE RAZAVI

Under the Direction of Steven T. Manson, PhD

ABSTRACT

The photoionization and structure of the superheavy elements No (Nobelium, Z=102), Cn (Copernicium, Z=112) and Og (Oganesson, Z=118) have been studied using Dirac-Fock (DF) and relativistic-random-phase approximation (RRPA) methods, respectively. The structure calculations reveal an unusual order of the inner-shell binding energies brought about by the relativistic effects, particularly the spin-orbit interaction, while the valence-shell structure of Cn is also anomalous owing to relativity. Photoionization cross sections and dipole photoelectron angular distributions were calculated from threshold to 35 a.u., 50 a.u. and 60 a.u. for the three atoms, respectively, and all subshells contributing to the total cross section in these energy regions have been considered. The resulting cross sections are dominated by interchannel coupling; the dominant subshell cross sections exerting very considerable influence upon the smaller cross sections. Using the feature of RRPA which allows us to omit particular couplings

among the photoionization channels, we are able to pinpoint the crucial coupling(s) in various situations. Finally, using the example of Cn, we have investigated the structure and photoionization of Cn confined in a C_{60} molecule, $Cn@C_{60}$, to study how a superheavy atom behaves under confinement conditions.

INDEX WORDS: Photoionization, Interchannel coupling, Superheavy atoms, Dirac-Fock, RRPA, Relativistic effects, Confined atoms

PHOTOIONIZATION AND STRUCTURE OF THE SUPERHEAVY ATOMS No, Cn AND Og

by

AHMAD KAFAEE RAZAVI

A Dissertation Submitted in Partial Fulfillment of the Requirements for the Degree of

Doctor of Philosophy

in the College of Arts and Sciences

Georgia State University

2021

PHOTOIONIZATION AND STRUCTURE OF THE SUPERHEAVY ATOMS No, Cn AND Og

by

AHMAD KAFAEE RAZAVI

Committee Chair: Steven T. Manson

Committee: Murad Sarsour

Brian D. Thoms

Vadym Apalkov

D. Mike Crenshaw

Electronic Version Approved:

Office of Graduate Services

College of Arts and Sciences

Georgia State University

May 2021

DEDICATION

I dedicate my dissertation work to my wife that the beginning of this course was after her encouragement and what I have done in this course was by her concomitance and camaraderie, as well as all my family, my parents and my children. Also, I dedicate my dissertation work to all people.

ACKNOWLEDGEMENTS

First, I would like to express my gratitude to God, the kindest that everything that I have is from him. Second, I would like to sincerely thank Dr. Manson for his best procedure in guidance, which encourages the students to reveal their creativity, and his patience and friendship. Also, all my fellows, graduate students, staff and professors of Physics Department in Georgia State University.

TABLE OF CONTENTS

LIST OF TABLES

LIST OF FIGURS

LIST OF ABBREVIATIONS

No – Nobelium

Cn – Copernicium

Og – Oganesson

HF – Hartree-Fock

DF – Dirac-Fock

RPA – Random Phase Approximation

RRPA – Relativistic Random Phase Approximation

Xe – Xenon

Hg – Mercury

Rn – Radon

Ra – Radium

CM – Cooper minima

HEG – Homogeneous electron gas

TDHF – Time-dependent Hartree-Fock equations

TDDF – Time-dependent Dirac-Fock equations

SOIAIC – Spin-orbit interaction activated interchannel coupling

1 INTRODUCTION

Atomic theory has undergone many changes in over the years. It evolved and extended from Bohr's 1913 suggestion of "stable energy levels" **[1]** to the present day. An important event was in 1905 with the special theory of relativity by Einstein [**2**]. The periodic table (Mendeleev) is strongly affected by relativity so that the behavior of some elements is peculiar. The color of gold and the fact that mercury is a liquid at room temperature are examples of the effect of relativity [**3**]. With increasing nuclear charge Z, relativity becomes more important regarding the deviation of elements' properties from nonrelativistic predictions. For example, including relativity, the valence orbital of copernicium, element 112, is *d* instead of *s*, even though it lies below mercury in the periodic table [**4**].

A superheavy element is an atom with atomic number greater than 100 [**5**]; these are not found in nature and can only be produced in particle accelerators [**6**]. They are ideal "laboratories" to study ultra-strong relativistic effects combined with the effects of many-body correlations [**5**]. To treat such atoms, it is essential for the quantum mechanical formulation to include relativistic interactions. Modern studies of atomic systems are generally conducted using quantum mechanics combined with relativity [**7**].

The heaviest element found in nature is uranium with atomic number 92. Atoms with higher Z than 92 must be created artificially. They are generally created in a collision between a beam of light atoms and a target of heavy atoms. And a new element is born by the fusion of light and heavy nuclei. The collision must be at high energy to overcome the repulsive force of the positive charges of the colliding nuclei, i.e., the energy must be large enough to overcome the Coulomb barrier. As the elements get heavier, the Coulomb barrier gets larger and larger. Experimentally, ^{252}No (Z = 102) nucleus is created by collisions of ^{48}Ca (Z=20) and $^{206\text{-}208}Pb$

(Z=82) after evaporating two to four neutrons from $^{254\text{-}256}$No. The processes may be repeated by radiating the projectiles, i.e. ^{48}Ca, into ^{238}U and ^{249}Cf for producing Cn (Z=112) and Og (Z=118) respectively [**8**].

In this work the calculations have been performed for the three superheavy atoms (No, Z = 102; Cn, Z = 112; and Og, Z = 118) with short half-lives and can be found only in particle accelerator. Nobelium lies below Yb in the periodic table [**5**], with half-life only 58 minutes [**9**] with most stable oxidation state +2 [**10**], and there is no subshell replacement. Copernicium is an extremely volatile substance, a gas or a liquid, with half-life only 29 seconds, and lies below Hg in the periodic table, but has rather different properties from its lighter homologues and more similarities with the noble gases such as radon. For example, because of relativistic effects, the valence shell is 6d, instead of 7s [**11**]. Oganesson is the heaviest known element, with the highest known atomic number, radioactive and very unstable, in the noble gas column. The half-life of Oganesson-294, the only confirmed isotope, is much less than one second (about 0.89 milliseconds) [**12**, **13**]. Because of its instability, very little experimental characterization of its properties is known, so theory is essential to gain an understanding of its atomic properties, and some of these properties are surprising. For example, unlike the lower-Z noble gases, Og is significantly reactive. Furthermore, all other members of the noble gas are, in fact, gases, but because of relativistic effects, it is predicted that Og is a solid and not a gas [**13**].

Aside from the basic level structure of the atoms, the response to ionizing electromagnetic radiation photoionization, is also a basic property of interest. The work tool is quantum mechanics theory. Max Planck introduced the idea that the energy of light is not a continuous wave-like phenomenon but a set of particles, called quanta, in explaining blackbody radiation [**14**]. The interaction of these quanta of light, called photons, with a target liberating and electron

(known as a photoelectron) is the process of photoionization. In this process, the photon is absorbed, and its energy is transferred to a bound of electron, causing the electron to be emitted, leaving behind a positive ion [**15**]. The probability of the photoabsorption process is embodied in the photoionization cross section. This cross section is strongly a function of the photon energy [**16**] and a primary purpose of the present work is to study this variation with energy for the three superheavy atoms, No, Cn and Og.

Around 1960's the thought of one-electron transaction in photoionization of atoms was replaced by the idea including the interactions of atomic electrons with each other, generally known as correlation. At first it was not thought to be of great importance, but subsequently, with more detailed investigations, it was found that the single-particle wave functions did not describe to situation very well. In other words, to obtain an accurate description of the photoionization process, it was necessary to realize that the behavior of the electrons in a multi-electron atom, molecule or condensed matter system is interdependent, i.e., they are correlated with each other. Therefore, for the calculation of the photoionization process, single particle wave function cannot well-represent either the initial or the final states since photoionization cannot be accurately described as one-electron process [**17**].

For the discrete initial state of an atomic photoionization process, a multiconfiguration (known also as configuration interaction) wave function can be used to incorporate the many-body aspects on the initial state. A similar type of wave function is used for the final continuum state, and the mixing of continuum wave functions, inherent in the idea of a multiconfiguration wave function, is known as interchannel coupling. Due to this mixing, the continuum wave function of a channel with a small cross section can mix with the wave function of a channel with a large cross section, thereby affecting the channel with the small cross section considerably

[**17**]. It is important to point out, as mentioned above, with increasing Z, relativity becomes more important, so that for superheavy atoms, studies of photoionization allow us to understand the interplay between relativistic and many-body interactions.

In addition to the cross section, there is also interest in the angular distribution asymmetry parameter for the photoionization of a given atomic subshell [**18**]. The photoionization cross section is related to the probability of photoelectron emission and depends on the absolute squares of the dipole matrix elements for the photoionizing transitions. The angular distribution asymmetry parameter is dependent on the ratio of the magnitudes of the various dipole matrix elements and their relative phases. Thus, the study of both the cross section and the asymmetry parameter for a given photoionization process yields complementary information. In particular, the cross section gives information about the strongest photoionization channels, while the asymmetry parameter β gives information about the ratios of the strengths of the various channels along with their phase differences [**19**, **20**].

It is also of interest to see how the properties of superheavy atoms behave in a confined environment [**22**]. In the last few decades, hollow carbon molecules known as fullerenes (after the architect R. Buckminster Fuller) have been used to confine atoms. The most notable member of the group is C_{60} that also has the virtue of being almost spherical. This near-spherical property of C_{60} simplifies the calculations and C_{60} is used in the work as the cage [**23**] using a spherical approximation. As an example of the effects of confinement on a superheavy atom, the structure and photoionization Cn confined in C_{60}, Cn@C_{60} are studied.

Over the years, studies of atomic photoionization, both experimental and theoretical, have demonstrated the importance electron correlation, especially the interaction between the residual ion and escaping electron, i.e., final state correlation and interchannel coupling [**24**]. The

predictions of the independent electron approximation are often different from experimental photoionization cross sections. It is well-established that the difference is quite significant at low photoelectron energies [**24**], but the present work shows even at higher energies, correlation can be extremely important.

Many-electron correlation effects have been studied by a number of theoretical techniques [**24**]. However, since we are dealing with superheavy atoms here, relativistic effects are crucial so the methodology employed must be relativistic, i.e., based on the Dirac equation. Thus, we employ a theoretical technique that contains both many-body correlation and relativistic interaction on an *ab initio* basis, the relativistic-random-phase approximation (RRPA) [**24**, **25**], a method that has been successfully applied to lower-Z atoms [**25**].

2 THEORY

2.1 Photoionization

A collision between a photon and anatom provides a condition such that an electron is released by absorbing the photon energy and then what remains is an ion. The photoionization cross section is a measure of the probability of ionization, since not all incident photons are absorbed.

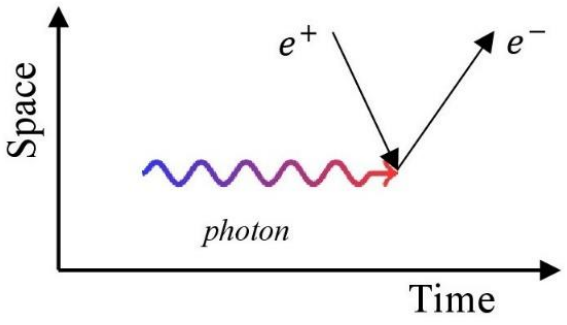

Figure 2.1: A simple Feynman diagram that shows Photoionization. (e^+) shows a hole [**26**].

The nonrelativistic Hamiltonian of an atom is [**27**]

$$H = \sum_{i=1}^{N}\left(\frac{p_i^2}{2m} - \frac{ze^2}{r_i}\right) + \sum_{i>j=1}^{N}\frac{e^2}{r_{ij}}, \tag{2.1}$$

The first term is the sum of potential energy which is the consequence of attractive force between the electrons and the nucleus and the kinetic energy. The second term is the repulsive potential energy between each pair of atomic electrons; *m* represents the electron mass, r_i is the position of the electron, e *is* the electron charge and $\hbar$ is Planck's constant, with the momentum operator $\vec{p} = -i\hbar\vec{\nabla}$. Finding the Hamiltonian owing to interaction with radiation requires extra terms, so $\vec{p}_i$ is substituted by $\vec{p}_i + \frac{|e|}{c}\vec{A}(\vec{r}_i, t)$ where $\vec{A}(\vec{r}_i, t)$ is the vector potential for the incident radiation field. The result is that the Hamiltonian becomes $(H + H_{int})$

$$H_{int} = \sum_{i=1}^{N}\left(\frac{|e|}{2mc}(\vec{p}_i \cdot \vec{A}(\vec{r}_i, t) + \vec{A}(\vec{r}_i, t) \cdot \vec{p}_i) + \frac{e^2}{2mc^2}\left|\vec{A}(\vec{r}_i, t)\right|^2\right), \tag{2.2}$$

where c is the speed of light. Considering Coulomb gauge, $\vec{\nabla}.\vec{A} = 0$, the form of the vector potential is given by [**22, 28**]

$$\vec{A}(\vec{r}_i, t) = \left(\frac{2\pi c^2\hbar}{\omega V}\right)^{\frac{1}{2}}\hat{\varepsilon}e^{i(\vec{k}\cdot\vec{r}_i - \omega t)}, \tag{2.3}$$

where V is the spatial volume (assuming box normalization) and $\hat{\varepsilon}$ is the direction of polarization, $\vec{k}$ is the wave vector and ω represents the angular frequency of the incident radiation. Now expanding $e^{i\vec{k}.\vec{r}_i}$ as

$$e^{i\vec{k}\cdot\vec{r}_i} \approx 1 + i\vec{k} \cdot \vec{r}_i - \cdots, \tag{2.4}$$

so that when the exponential $\vec{k} \cdot \vec{r}_i$ is small compared to unity, which it is for photon energies below about 10 keV, then the exponential can be approximated by 1; this is known as the dipole approximation. Thus, taking $e^{i\vec{k}\cdot\vec{r}_i} \approx 1$ we then have [**22**]

$$H_{int} = \frac{|e|}{mc}\left(\frac{2\pi c^2\hbar}{\omega V}\right)^{\frac{1}{2}}\sum_{i=1}^{N}\hat{\varepsilon}\cdot\vec{p}_i\, e^{-i\omega t}. \qquad (2.5)$$

2.2 Many-Body interactions theory, Second Quantization

In quantum mechanics, concerning the interaction between electromagnetic field and particles, the particles are quantized while electromagnetic field remains classical. An accurate description requires quantization of both. Therefore, it requires reformulating in quantum mechanics that leads us to consider both particles and electromagnetism in terms of quantum fields. This procedure and idea is known as the quantum field theory or the second quantization [**29**].

In this theory aphotonis treated as a quantized excitation of a field. Maxwell's classical electromagnetic field was quantized by Dirac, termed relativistic quantum field theory, and the interaction between electron and photon is the interaction between quantized excitations of two quantum fields [**29**]. This involves two operators, creation and annihilation (destruction) operators. One of the best examples for describing these two operators is harmonic oscillator. We begin with the Hamiltonian [**30**]

$$\widehat{H} = \frac{\hat{p}^2}{2m} + \frac{1}{2}k\hat{x}^2 = \frac{\hat{p}^2}{2m} + \frac{1}{2}m\omega^2\hat{x}^2, \qquad (2.6)$$

containing kinetic and potential energy; *m* represents the particle's mass, *k* is the force constant, $\omega = \sqrt{\frac{k}{m}}$ is the angular frequency of the oscillator, $\hat{p}$ and $\hat{x}$ are momentum and position operators, respectively, and they are related by the equation ($\hat{p} = -i\hbar\frac{\eth}{\eth x}$). Considering energy levels $\left(E_n = \hbar\omega\left(n + \frac{1}{2}\right)\right)$, two ladder operators, annihilation and creation (respectively) are defined as

$$a = \sqrt{\frac{m\omega}{2\hbar}}\left(\hat{x} + \frac{i}{m\omega}\hat{p}\right), \tag{2.7}$$

$$a^{\dagger} = \sqrt{\frac{m\omega}{2\hbar}}\left(\hat{x} - \frac{i}{m\omega}\hat{p}\right), \tag{2.8}$$

After some calculation for a system containing only one- and two-body interactions, we obtain the Hamiltonian ($H = H_1 + H_2$) in second quantization [**31**]

$$\mathrm{H} = \sum_i \sum_j a_i^{\dagger}\langle i|f|j\rangle a_j + \frac{1}{2}\sum_i \sum_j \sum_k \sum_l a_i^{\dagger} a_j^{\dagger}\langle ij|V|kl\rangle a_l\, a_k, \tag{2.9}$$

where

$$\langle ij|V|kl\rangle = \int dq_1 \int dq_1 \phi_i^*(q_1)\phi_j^*(q_2)V(q_1, q_2)\phi_k(q_1)\phi_l(q_2), \tag{2.10}$$

now comparing the Hamiltonian ($H = H_1 + H_2$) with first quantization,

$$\mathrm{H} = \sum_{i=1}^{N} f(q_i) + \frac{1}{2}\sum_{j=1, j\neq i}^{N}\sum_{j=1}^{N} V(q_i, q_j)\ ,\ \ f(q_i) = -\frac{1}{2}\nabla_i^2 - \frac{z}{r_i}\,. \tag{2.11}$$

in atomic units for a hydrogenic system of charge Z.

2.3 Dirac equation

The Dirac equation is a fundamental step in the history of physics. The method incorporates quantum mechanics with special relativity. As a result, electron spin and the existence of anti-matter were described [**32**]. This equation incorporated the spin coordinates that Pauli predicted, an additional quantum degree of freedom for the electron, spin coordinates [**33**].

The equation was formulated by **Dirac** regarding an important principle in physics that the equations should be of the same form under Lorentz transformations. Also, the result was compatible with the Stern–Gerlach experiment, done a few years earlier [**34**]. The Klein-Gordon equation, formulated earlier, also included the negative energy solutions, but couldn't made to be compatible with electron spin, [**34**].

Taking $E \rightarrow i\hbar\frac{\partial}{\partial t}$ and $\vec{\mathrm{p}} \rightarrow i\hbar\vec{\nabla}$ the relativistic equation for energy [**35**]

$$E^2 = |\vec{p}|^2c^2 + m^2c^4, \tag{2.12}$$

one obtains the Klein-Gordon (KG) equation

$$-\hbar^2\frac{\partial^2\psi}{\partial t^2} = -\hbar^2c^2\nabla^2\psi + m^2c^4\psi, \tag{2.13}$$

and, using the notation

$$\partial_\mu \equiv \frac{\partial}{\partial x^\mu} = (\frac{\partial}{\partial t}, \frac{\partial}{\partial x}, \frac{\partial}{\partial y}, \frac{\partial}{\partial z}) \rightarrow \partial^\mu\partial_\mu \equiv (\frac{\partial^2}{\partial t^2}, -\frac{\partial^2}{\partial x^2}, -\frac{\partial^2}{\partial y^2}, -\frac{\partial^2}{\partial z^2})$$

the KG equation in can be written (in atomic units) in a compact form as

$$\left(\partial^\mu\partial_\mu + m^2\right)\psi = 0. \tag{2.14}$$

for plane wave solutions, $\psi = Ne^{i(\vec{p}.\vec{r}-Et)}$ the KG equation gives

$$-E^2\psi = -|\vec{p}|^2c^2\psi - m^2c^4\psi, \tag{2.15}$$

$$E = \pm\sqrt{|\vec{p}|^2c^2 + m^2c^4}, \tag{2.16}$$

and the probability and current density are [**35**]

$$\rho = i\left(\psi^*\frac{\partial\psi}{\partial t} - \psi\frac{\partial\psi^*}{\partial t}\right), \quad \text{and} \quad \vec{j} = i\left(\psi^*\vec{\nabla}\psi - \psi\vec{\nabla}\psi^*\right), \tag{2.17}$$

calculated using a plane wave $\psi = Ne^{i(\vec{p}.\vec{r}-Et)}$ with the number of particles per unit volume $|N|^2$, therefore,

$$\rho = 2E|N|^2, \quad \text{and} \quad \vec{j} = |N|^2\vec{p}. \tag{2.18}$$

The inability of the Klein-Gordon equation to deal with electron spin motivated Dirac to improve the calculation by a different formulation of the relativistic problem that could describe the intrinsic spin and magnetic moment of the electron [**35**].

Dirac proposed the equation, based on the Klein–Gordon and Schrödinger wave equations, and also the Lorentz transformations [**34**]

$$(i\hbar\frac{\partial}{\partial t} + i\hbar c\vec{\alpha}\cdot\vec{\nabla})\psi = \beta mc^2\psi, \tag{2.19}$$

where *m* is the particle's mass. Two other parameters, the scalar parameter β and vector parameter $\vec{\alpha}$, appeared in the Dirac equation. Imposing the requirement that the relativistic mass-energy formula, Eq. (2.12) must be satisfied yields

$$\alpha_x^2 = \alpha_y^2 = \alpha_z^2 = \beta^2 = 1, \tag{2.20}$$

$$\alpha_i\beta + \beta\alpha_j = 0, \tag{2.21}$$

$$\alpha_j\alpha_k + \alpha_k\alpha_j = 0, \qquad (j \neq k), \tag{2.22}$$

so that α_j and β cannot be numbers; instead, they must be (at least) 4×4 matrixes. Therefore, the wave function is introduced as a four-component Dirac Spinor [**35**].

$$\psi = \begin{pmatrix}\psi_1\\ \psi_2\\ \psi_3\\ \psi_4\end{pmatrix}, \tag{2.23}$$

this new wave function involves new degrees of freedom. The Hamiltonian (H_D) must be Hermitian, which requires four anti-commuting Hermitian 4×4 matrixes.

$$\alpha_x = \alpha_x^\dagger; \quad \alpha_y = \alpha_y^\dagger; \quad \alpha_z = \alpha_z^\dagger; \quad \beta = \beta^\dagger, \tag{2.24}$$

so that $\vec{\alpha}$, β can be determined. The best choice is formulation based on the Pauli spin matrixes

$$\beta = \begin{pmatrix}I & 0\\ 0 & -I\end{pmatrix}, \qquad \alpha_j = \begin{pmatrix}0 & \sigma_j\\ \sigma_j & 0\end{pmatrix}, \tag{2.25}$$

with $$I = \begin{pmatrix}1 & 0\\ 0 & 1\end{pmatrix}, \quad \sigma_x = \begin{pmatrix}0 & 1\\ 1 & 0\end{pmatrix}, \quad \sigma_y = \begin{pmatrix}0 & -i\\ i & 0\end{pmatrix}, \quad \sigma_z = \begin{pmatrix}1 & 0\\ 0 & -1\end{pmatrix}. \tag{2.26}$$

The matrices anti-commute with each other, also all matrices are Hermitian. Now a new formation of Dirac equation with four Dirac gamma matrixes [**35**]

$$\gamma^0 \equiv \beta; \quad \gamma^1 \equiv \beta\alpha_x; \quad \gamma^2 \equiv \beta\alpha_y; \quad \gamma^3 \equiv \beta\alpha_z, \tag{2.27}$$

the gamma matrixes may be written in the way of Pauli-Dirac representation:

$$\gamma^0 = \begin{pmatrix} \mathrm{I} & 0 \\ 0 & \mathrm{I} \end{pmatrix}; \quad \gamma^{\mathrm{k}} = \begin{pmatrix} 0 & \sigma_k \\ \sigma_k & 0 \end{pmatrix}, \tag{2.28}$$

or, the representation in full,

$$\gamma^0 = \begin{pmatrix} 1 & 0 & 0 & 0 \\ 0 & 1 & 0 & 0 \\ 0 & 0 & -1 & 0 \\ 0 & 0 & 0 & -1 \end{pmatrix}; \quad \gamma^1 = \begin{pmatrix} 0 & 0 & 0 & 1 \\ 0 & 0 & 1 & 0 \\ 0 & -1 & 0 & 0 \\ -1 & 0 & 0 & 0 \end{pmatrix}; \quad \gamma^2 = \begin{pmatrix} 0 & 0 & 0 & -i \\ 0 & 0 & i & 0 \\ 0 & i & 0 & 0 \\ -i & 0 & 0 & 0 \end{pmatrix};$$

$$\gamma^3 = \begin{pmatrix} 0 & 0 & 1 & 0 \\ 0 & 0 & 0 & -1 \\ -1 & 0 & 0 & 0 \\ 0 & 1 & 0 & 0 \end{pmatrix}. \tag{2.29}$$

Considering a free particle solution ($\psi = u(E,\vec{p})e^{i(\vec{p}.\vec{r}-Et)}$), which $u(E,\vec{p})$ is a constant four-component spinor the derivatives are

$$\partial_0\psi = \frac{\partial\psi}{\partial t} = -iE\psi; \quad \partial_1\psi = \frac{\partial\psi}{\partial t} = -ip_x\psi, \quad \ldots\ldots \tag{2.30}$$

and the result after substituting into the Dirac equation

$$(\gamma^0 E - \gamma^1 p_x - \gamma^2 p_y - \gamma^3 p_z - m)u = 0, \tag{2.31}$$

we get a Dirac equation in momentum space, that contains no derivatives.

$$\left(\gamma^\mu p_\mu - m\right)\psi = 0. \tag{2.32}$$

Eq. (2.31) changes as follows when the particle is at rest ($\vec{p} = 0$ and $\psi = u(E,0)e^{-iEt}$),

$$E\gamma^0 u - mu = 0 \quad \rightarrow \quad E\begin{pmatrix} 1 & 0 & 0 & 0 \\ 0 & 1 & 0 & 0 \\ 0 & 0 & -1 & 0 \\ 0 & 0 & 0 & -1 \end{pmatrix}\begin{pmatrix} \Phi_1 \\ \Phi_2 \\ \Phi_3 \\ \Phi_4 \end{pmatrix} = m\begin{pmatrix} \Phi_1 \\ \Phi_2 \\ \Phi_3 \\ \Phi_4 \end{pmatrix}, \tag{2.33}$$

and these four orthogonal column matrices are the solutions

$$u_1(m,0) = \begin{pmatrix} 1 \\ 0 \\ 0 \\ 0 \end{pmatrix}; \quad u_2(m,0) = \begin{pmatrix} 0 \\ 1 \\ 0 \\ 0 \end{pmatrix}; \quad u_3(m,0) = \begin{pmatrix} 0 \\ 0 \\ 1 \\ 0 \end{pmatrix}; \quad u_4(m,0) = \begin{pmatrix} 0 \\ 0 \\ 0 \\ 1 \end{pmatrix}. \tag{2.34}$$

where u_1 and $u_2 \rightarrow E = m$; u_3 and $u_4 \rightarrow E = -m$.

The time dependent form of wave function ($\psi = u(E,0)e^{-iEt}$) is

$$\psi_1 = \begin{pmatrix}1\\0\\0\\0\end{pmatrix} e^{-imt}; \quad \psi_2 = \begin{pmatrix}0\\1\\0\\0\end{pmatrix} e^{-imt}; \quad \psi_3 = \begin{pmatrix}0\\0\\1\\0\end{pmatrix} e^{+imt}; \quad \psi_4 = \begin{pmatrix}0\\0\\0\\1\end{pmatrix} e^{+imt}. \qquad (2.35)$$

where ψ_1 and ψ_2 are two spin states with E > 0, ψ_3 and ψ_4 are two spin states with E < 0.

The next step is solving Dirac equation for the general plane wave function, considering $\psi = u(E,\vec{p})e^{i(\vec{p}.\vec{r}-Et)}$, and, starting with Eq. (2.30) and (2.31)

$$\gamma^{\mu}p_{\mu} - m = \begin{pmatrix}\mathrm{I} & 0\\ 0 & -\mathrm{I}\end{pmatrix} E - \begin{pmatrix}0 & \vec{\sigma}\\ -\vec{\sigma} & 0\end{pmatrix}.\vec{p} - m\begin{pmatrix}\mathrm{I} & 0\\ 0 & \mathrm{I}\end{pmatrix} = \begin{pmatrix}(\mathrm{E}-\mathrm{m})\mathrm{I} & -\vec{\sigma}.\vec{p}\\ \vec{\sigma}.\vec{p} & -(\mathrm{E}+\mathrm{m})\mathrm{I}\end{pmatrix}, \qquad (2.36)$$

To continue the process, $u = \begin{pmatrix}u_A\\u_B\end{pmatrix}$

$$u(\gamma^{\mu}p_{\mu} - m) = 0, \ \rightarrow \begin{pmatrix}(\mathrm{E}-\mathrm{m})\mathrm{I} & -\vec{\sigma}.\vec{p}\\ \vec{\sigma}.\vec{p} & (-\mathrm{E}-\mathrm{m})\mathrm{I}\end{pmatrix}\begin{pmatrix}u_A\\u_B\end{pmatrix} = \begin{pmatrix}0\\0\end{pmatrix}, \qquad (2.37)$$

$$\begin{cases}(\vec{\sigma}.\vec{p})u_B = (\mathrm{E}-\mathrm{m})u_A\\ (\vec{\sigma}.\vec{p})u_A = (\mathrm{E}+\mathrm{m})u_B\end{cases} \rightarrow \ u_B = \frac{\vec{\sigma}.\vec{p}}{E+m}u_A = \frac{1}{E+m}\begin{pmatrix}p_z & p_x - ip_y\\ p_x + ip_y & p_z\end{pmatrix}u_A. \qquad (2.38)$$

Now defining u_A (u_1 and u_2) for E > 0, ($E = +\left|\sqrt{|\vec{p}|^2 + m^2}\right|$), and correspondingly, u_B (u_3 and u_4) for E < 0, ($E = -\left|\sqrt{|\vec{p}|^2 + m^2}\right|$), then obtain four solutions of form [**35**], $\psi_i = u_i(E,\vec{p})e^{i(\vec{p}.\vec{r}-Et)}$ representing positive energy, a particle,

$$u_1 = N\begin{pmatrix}1\\0\\\frac{p_z}{\mathrm{E}+\mathrm{m}}\\\frac{p_x+ip_y}{E+m}\end{pmatrix}; \ u_2 = N\begin{pmatrix}0\\1\\\frac{p_x-ip_y}{\mathrm{E}+\mathrm{m}}\\\frac{-p_z}{E+m}\end{pmatrix}; \ u_3 = N\begin{pmatrix}\frac{p_z}{\mathrm{E}-\mathrm{m}}\\\frac{p_x+ip_y}{E-m}\\1\\0\end{pmatrix}; u_4 = N\begin{pmatrix}\frac{p_x-ip_y}{\mathrm{E}-\mathrm{m}}\\\frac{-p_z}{E-m}\\0\\1\end{pmatrix}, \qquad (2.39)$$

$$u_1, u_2 \rightarrow \ E = +\left|\sqrt{|\vec{p}|^2 + m^2}\right|; \qquad u_3, u_4 \ \rightarrow \ E = -\left|\sqrt{|\vec{p}|^2 + m^2}\right|,$$

and four solutions of form $\psi_i = v_i(E,\vec{p})e^{-i(\vec{p}.\vec{r}-Et)}$ for negative energy representing an anti-particle,

$$v_1 = N\begin{pmatrix} \frac{p_x - ip_y}{E+m} \\ \frac{-p_z}{E+m} \\ 0 \\ 1 \end{pmatrix};\ v_2 = N\begin{pmatrix} \frac{p_z}{E+m} \\ \frac{p_x + ip_y}{E+m} \\ 1 \\ 0 \end{pmatrix};\ v_3 = N\begin{pmatrix} 1 \\ 0 \\ \frac{p_z}{E-m} \\ \frac{p_x + ip_y}{E-m} \end{pmatrix};\ v_4 = N\begin{pmatrix} 0 \\ 1 \\ \frac{p_x - ip_y}{E-m} \\ \frac{-p_z}{E-m} \end{pmatrix}. \qquad (2.40)$$

$$v_1, v_2 \rightarrow\ \ E = +\left|\sqrt{|\vec{p}|^2 + m^2}\right|;\qquad v_3, v_4\ \ \rightarrow\ \ E = -\left|\sqrt{|\vec{p}|^2 + m^2}\right|,$$

The change of the sign of the power of exponential function is interpreted as the existence of an anti-particle, which was predicted by Dirac equation. Therefore, when we focus on the positive energy region the solution is four component spinor (u_1,u_2,v_1,v_2) and in negative energy it is (u_3,u_4,v_3,v_4) [**35**].

Now looking at orbital angular momentum ($L = \vec{r} \times \vec{p}$), and the fact that does not commute with the Hamiltonian, means that it is not a constant of motion.

$$\left[H, \vec{L}\right] = [\vec{\alpha} \cdot \vec{p} + \beta m, \vec{r} \times \vec{p}\ ] = [\vec{\alpha} \cdot \vec{p}, \vec{r} \times \vec{p}\ ] = -i\vec{\alpha} \times \vec{p}. \qquad (2.41)$$

However, a new 4×4 operator is introduced,

$$\vec{S} = \frac{1}{2}\vec{\Sigma} = \frac{1}{2}\begin{pmatrix} \vec{\sigma} & 0 \\ 0 & \vec{\sigma} \end{pmatrix}, \qquad (2.42)$$

where the Pauli spin matrixes are given by $\vec{\sigma}$. The components are

$$\Sigma_x = \begin{pmatrix} 0 & 1 & 0 & 0 \\ 1 & 0 & 0 & 0 \\ 0 & 0 & 0 & 1 \\ 0 & 0 & 1 & 0 \end{pmatrix};\ \ \Sigma_y = \begin{pmatrix} 0 & -i & 0 & 0 \\ i & 0 & 0 & 0 \\ 0 & 0 & 0 & -i \\ 0 & 0 & i & 0 \end{pmatrix};\ \ \Sigma_x = \begin{pmatrix} 1 & 0 & 0 & 0 \\ 0 & -1 & 0 & 0 \\ 0 & 0 & 1 & 0 \\ 0 & 0 & 0 & 1 \end{pmatrix}, \qquad (2.43)$$

and the commutator with this new operator

$$\left[H, \vec{\Sigma}\right] = \left[\vec{\alpha} \cdot \vec{p} + \beta m, \vec{\Sigma}\ \right] = 2i\vec{\alpha} \times \vec{p}, \qquad (2.44)$$

which is also not a constant of the motion. However,

$$\left[H, \vec{\mathrm{S}}\right] = \frac{1}{2}\left[H, \vec{\Sigma}\right] = i\vec{\alpha} \times \vec{p} = -\left[H, \vec{\mathrm{L}}\right], \qquad (2.45)$$

so that

$$\left[H, \vec{\mathrm{L}} + \vec{\mathrm{S}}\ \right] = 0, \qquad (2.46)$$

so the $\vec{J} = \vec{L} + \vec{S}$ is a constant of the motion. For both $\vec{S}$ and $\vec{\sigma}$ the commutation relationships are the same, for example

$$\left[\sigma_x \sigma_y\right] = i\sigma_z \; ; \quad \left[S_x, S_y\right] = iS_z, \tag{2.47}$$

and both S^2 and S_z are diagonal.

$$S^2 = \frac{1}{4}\left(\Sigma_x^2 + \Sigma_y^2 + \Sigma_z^2\right) = \frac{3}{4}\begin{pmatrix} 1 & 0 & 0 & 0 \\ 0 & 1 & 0 & 0 \\ 0 & 0 & 1 & 0 \\ 0 & 0 & 0 & 1 \end{pmatrix}; \quad S_z = \frac{1}{2}\begin{pmatrix} 1 & 0 & 0 & 0 \\ 0 & -1 & 0 & 0 \\ 0 & 0 & 1 & 0 \\ 0 & 0 & 0 & -1 \end{pmatrix}. \tag{2.48}$$

Consequently, the Dirac equation includes the intrinsic angular momentum of fermions because the matrix (operator) $\vec{S}$ has all the properties of angular momentum. The magnetic moment for electrons, fermions, which are the subject of this investigation, is shown to be [**35**]

$$\vec{\mu} = \frac{q}{m}\overrightarrow{S}. \tag{2.49}$$

It is noteworthy that the spinors u_1, u_2, v_1, v_2 are not eigenstates of S_z in general, but only for those travelling particles (or anti-particles) in the z-direction, means ($p_x = p_y = 0 \rightarrow p_z = \pm|\vec{p}|$. Therefore, the eigenstates of S_z are given as

$$u_1 = N\begin{pmatrix} 1 \\ 0 \\ \frac{\pm|\vec{p}|}{\mathrm{E+m}} \\ 0 \end{pmatrix}; \; u_2 = N\begin{pmatrix} 0 \\ 1 \\ 0 \\ \frac{\mp|\vec{p}|}{E+m} \end{pmatrix}; \; v_1 = N\begin{pmatrix} 0 \\ \frac{\mp|\vec{p}|}{E+m} \\ 0 \\ 1 \end{pmatrix}; \; v_2 = N\begin{pmatrix} \frac{\pm|\vec{p}|}{E+m} \\ 0 \\ 1 \\ 0 \end{pmatrix}, \tag{2.50}$$

which results in

$$\begin{cases} S_z u_1 = +\frac{1}{2}u_1 & ; \quad S_Z^v v_1 = -S_z v_1 = +\frac{1}{2}v_1 \\ S_z u_1 = -\frac{1}{2}u_1 & ; \quad S_Z^v v_1 = -S_z v_1 = -\frac{1}{2}v_1 \end{cases}. \tag{2.51}$$

Note the behavior of S_z as an operator; the signs are different for dealing with particle or anti-particle spinors [**35**]. Spin is a phenomenon that is explained mathematically within the framework of quantum mechanics and cannot be described classically [**36**].

2.4 Dirac-Fock method

Pursuing the attempt to generalize the quantum theory by involving relativity, **Dirac** brought up a system as an electron, that is the host of an incident wave, then the emitted radiation was calculated by employing the matrix elements. A special explanation was proposed by **Fock** (the Fock space) in conventional language of quantum mechanics and became important for the method's generalization. Based on his idea, the translation of the formalism of second quantization is allowed at any stage. Relativistic wave equations were added by Fock and **Podolsky** for electrons and the electromagnetic field, instead of scalar field. Fock attempted to formulate the two electrons' retarding interaction in the approximation of the order of $(v/c)^2$ [**37**].

A brief description of the Hartree–Fock method (HF) clarifies the necessity for some developments after introducing the Schrödinger equation. In this method the equations were formulated by converting the Laplacian from Cartesian to spherical coordinates and the wave function has two parts, radial function (p(r)/r) multiplied by spherical harmonic [**38**].

$$\psi_i = (1/r)P_{n_i l_i}(r)Y_{l_i m_l}(\theta,\phi)\sigma_{m_s}(s_z), \qquad (2.52)$$

In a system consist of N electrons in N states, considering Independent Particle Model the wavefunction is proportional to the multiplication of all single wavefunctions [**38**]

$$\Psi(x_1, x_2, x_3, \dots, x_N) = \psi_\alpha(x_1)\psi_\beta(x_2)\psi_\gamma(x_3)\dots\psi_\upsilon(x_N), \qquad (2.53)$$

There are some reasons that Hartree method needed some variations and improvements. For example, the wavefunction for Fermions is anti-symmetric while it is disregarded in Hartree method [**39**]. The next step that was taken in Hartree–Fock method is solving the Fermions' anti-symmetric problem included spin in the wavefunction [**39**]. By neglecting electron correlations, we may assume this method as "Frozen Orbital Approximation" or "Independent Particle

Approximation" that is a portion of the ionization energy, which means other orbitals do not vary and retained frozen during the process [**38, 40**]. Therefore, instead of N different wavefunctions for an N electron atom (Eq. 2.53) Slater determinant is the method for calculation [**40**].

$$\psi^{(N)} = \frac{1}{\sqrt{N!}}\begin{vmatrix} u_1(q_1) & u_1(q_2) & \dots\dots & u_1(q_N) \\ u_2(q_1) & \dots\dots\dots & \dots\dots & \dots\dots \\ \dots\dots & \dots\dots\dots & u_i(q_j) & \dots\dots \\ u_N(q_1) & \dots\dots\dots & \dots\dots & u_N(q_N) \end{vmatrix}, \qquad (2.54)$$

the simplest example is Helium. It displays a system with only two electrons so $\psi^{(2)}$ is

$$\psi^{(2)} = \psi(q_1, q_2) = \frac{1}{\sqrt{2}}\begin{vmatrix} u_1(q_1) & u_1(q_2) \\ u_2(q_1) & u_2(q_2) \end{vmatrix} = \frac{1}{\sqrt{2}}[u_1(q_1)u_2(q_2) - u_1(q_2)u_2(q_1)], \qquad (2.55)$$

Equation 2.55 has two parts $\frac{1}{\sqrt{2}}[1-2]$, Considering spin as ν, then we have: $\psi(q_1, q_2) = \phi(q_1, q_2)\nu_s(\uparrow,\downarrow)$. By the assumption that q_1 is at $\vec{r}_1$ and q_2 is at $\vec{r}_2$, now coulomb and exchange interaction integrals may be introduced [**41**]

$$U_{11} = \int\int d^3\vec{r}_1\, d^3\vec{r}_2 \varphi_1^*(\vec{r}_1)\varphi_2^*(\vec{r}_2)\frac{1}{r_{12}}\varphi_1(\vec{r}_1)\varphi_2(\vec{r}_2) = J, \qquad \text{coulomb} \qquad (2.56)$$

$$U_{21} = \int\int d^3\vec{r}_1\, d^3\vec{r}_2 \varphi_1^*(\vec{r}_2)\varphi_2^*(\vec{r}_1)\frac{1}{r_{12}}\varphi_1(\vec{r}_1)\varphi_2(\vec{r}_2) = K, \qquad \text{exchange} \qquad (2.57)$$

showing as a matrix

$$\mathbf{U} = \begin{vmatrix} J & K \\ K^* & J^* \end{vmatrix}. \qquad \begin{matrix} J : \text{Coulomb} \\ K : \text{Exchange} \end{matrix} \qquad (2.58)$$

Considering the determinant, for high Z atom, solving the problem is impossible. In 1948, in a paper, **Hartree** gives an example about the element Fe, which it requires 10^{78} entries for full tabulation [**38**]. Therefore, there have been several attempts to make the procedure solvable. In this investigation the Hartree–Fock method was chosen to calculate the binding energies for all subshells of three elements No, Cn and Og. Following is a brief explanation. The complete Hamiltonian is the sum of the Hamiltonians of the radiation field, H_{rad}, the atomic electrons, H_{el}, and the interaction between them, H_{int},

$$H = H_{rad} + H_{el} + H_{int}, \tag{2.59}$$

where H_{rad} is the sum of two integrals of electric and magnetic fields

$$H_{rad} = \frac{1}{8\pi}\int (\left|\vec{E}\right|^2 + \left|\vec{H}\right|^2), \tag{2.60}$$

and we may rewrite Eq. (2.2) with Dirac notation

$$H_{int} = -\sum_k e_k\left(\vec{\alpha}_k \cdot \vec{A}(k)\right), \tag{2.61}$$

and the Hamiltonian (H_{el}) as mentioned in Eq. (2.41)

$$H_{el} = \sum_k (\vec{\alpha}_k \cdot \vec{P}_k + \beta_k m_k). \tag{2.62}$$

Considering free atom while there are no external fields, $H_{rad} = 0$ and $H_{int} \ll H_{el}$. Beginning by a simple example, supposing an electron inside the field of nucleus and under effect of time averaged field of $\underline{N-1}$ other electrons, so one-electron wavefunction by the spherically symmetric potential approximation is [**38**]

$$\psi_{nlm_l m_s} = (1/r)P_{n_i l_i}(r)Y_{l_i m_l}(\theta,\phi)\sigma_{m_s}(s_z), \tag{2.63}$$

while electron correlation in ignored (exchange, regarding Eq. 2.56). Now moving toward Variational Quantum Algorithms (VQAs), the variation of the average energy is

$$E_{av} = \frac{\int \Psi^* H \Psi}{\int \Psi^* \Psi}, \tag{2.64}$$

by orthogonality

$$\int_0^\infty P^*_{n_i l_i}(r)P_{n_j l_i}(r)dr = \delta_{n_j n_i}, \tag{2.65}$$

integrating out the angular and spin parts, the variational expression is obtained [**38**]

$$\delta\left\{E_{av} - \sum_{j=1}^{N}\epsilon_j w_j \int_0^\infty P_j^* P_j\, d(r) - \sum_{i\neq j}^{N}\delta_{j_j l_i} w_j w_i \int_0^\infty P_j^* P_j\, d(r)\right\} = 0, \tag{2.66}$$

and the potential (self-consistent field) ψ_i $(i = 1, N)$

$$V_i = \int \frac{\rho}{r} d^3(r) = \sum_{j \neq i}^{N} e \int \frac{|\psi_j|^2}{r_{ij}} d^3(r), \tag{2.67}$$

then the Schrödinger Equation

$$\left(\frac{\nabla_i^2}{2} - \frac{z}{r_i} + V_i\right)\psi_i = \epsilon_i \psi_i. \tag{2.68}$$

Now some important equations are shown, considering the following expansion

$$\frac{1}{r_{ij}} = \frac{1}{|\vec{r}_i - \vec{r}_j|} = \sum_{0}^{\infty} \frac{r_<^k}{r_>^{k+1}} P_k(\cos\theta)$$

spherically averaged atom results Hartree-Fock equation [**38**]

$$\left[-\frac{d^2}{dr^2} + \frac{l_i(l_i+1)}{r^2} - \frac{2z}{r} + \sum_{j(\neq i)=1}^{N} w_j \int_0^{\infty} \frac{2}{r_>} P_j^2(r^2) dr^2 - (w_i - 1)A_i(r)\right] P_i(r) =$$

$$\epsilon_i P_i(r) + \sum_{j(\neq i)=1}^{N} w_j \left[\delta_{l_i l_j} \epsilon_{ij} + B_{ij}(r)\right] P_j(r), \tag{2.69}$$

$A_i(r)$ and $B_{ij}(r)$ are Hartree-Fock local and non-local potentials, respectively.

$$A_i(r) = \frac{2l_i + 1}{4l_i + 1} \sum_{k>0} \begin{pmatrix} l_i & k & l_i \\ 0 & 0 & 0 \end{pmatrix}^2 \int_0^{\infty} \frac{2r_<^k}{r_>^{k+1}} P_i^2(r_2) dr_2, \tag{2.70}$$

$$B_{ij}(r) = \frac{1}{2} \sum_{k} \begin{pmatrix} l_i & k & l_i \\ 0 & 0 & 0 \end{pmatrix}^2 \int_0^{\infty} \frac{2r_<^k}{r_>^{k+1}} P_j(r_2) P_i^2(r_2) dr_2, \tag{2.71}$$

next step, using Dirac-Coulomb Hamiltonian

$$H = \sum_i \left[c\vec{\alpha}_i . \vec{P}_i + c^2(\beta_i - 1) - \frac{Ze^2}{r_j}\right] + \sum_{i>j} \frac{e^2}{r_{ij}}, \tag{2.72}$$

and then Dirac-Hartree-Fock equations

$$c\frac{dQ_a}{dr}-\frac{ck}{r}Q_a-\frac{Z}{r}P_a+\sum_{b,k}\left[C^k(ab)P_a\frac{1}{r}Y_k(bb)+D^k(ab)P_b\frac{1}{r}Y_k(bb)\right]=$$

$$\epsilon_{aa}P_a+\sum_{b\neq a}qb\,\epsilon_{ab}P_b\,, \tag{2.73}$$

$$-c\frac{dP_a}{dr}-\frac{ck}{r}P_a-2c^2Q_a-\frac{Z}{r}Q_a++\sum_{b,k}\left[C^k(ab)Q_a\frac{1}{r}Y_k(bb)+D^k(ab)Q_b\frac{1}{r}Y_k(bb)\right]=$$

$$\epsilon_{aa}P_a+\sum_{b\neq a}qb\,\epsilon_{ab}P_b. \tag{2.74}$$

Solving one-electron Dirac-Fock equation, $P_{nk}(r)$ and $Q_{nk}(r)$ are the large and small components, respectively, of one-electron radial wavefunction, and as a self-consistent-field solution. The product of one-electron Dirac orbitals is displayed by a Slater determinant

$$|nkm\rangle=\frac{1}{r}\begin{pmatrix}P_{nk}(r)\chi_{km}(\hat{r})\\ iQ_{nk}(r)\chi_{-km}(\hat{r})\end{pmatrix}, \tag{2.75}$$

in lsj coupling plot, χ is the spinor spherical harmonic [**38**]

$$\chi_{km}(\hat{r})=\chi_{km}(\theta,\varphi,\sigma)=\sigma_{ms}\left\langle lm-m_s\frac{1}{2}m_s\middle|l\frac{1}{2}jm\right\rangle Y_{lm-m_s}(\theta,\varphi)\xi_{ms}(\sigma). \tag{2.76}$$

Taking the one-particle relativistic Dirac Hamiltonian, a lower bound for the ground state energy may be called no-pair operator [**42**], so we can write [**38**]

$$H^{nopair}=\sum_{i=1}^{N}H_D(r_i)+\sum_{i<j}v\left(\left|\vec{r}_i-\vec{r}_j\right|\right), \tag{2.77}$$

where H_D represents the one electron Dirac operator and the electron-electron interaction of order α (one-photon exchange) is shown by v. Therefore, in Coulomb gauge v_{ij} is formulated by

$$v_{ij}=\frac{1}{r_{ij}}-\frac{\vec{\alpha}_i.\vec{\alpha}_j}{r_{ij}}-\frac{\vec{\alpha}_i.\vec{\alpha}_j}{r_{ij}}\left[\cos\left(\frac{w_{ij}r_{ij}}{c}\right)-1\right]-c^2\left(\vec{\alpha}_i\cdot\vec{\nabla}_i\right)\left(\vec{\alpha}_j\cdot\vec{\nabla}_j\right)\frac{\cos\left(\frac{w_{ij}r_{ij}}{c}\right)-1}{w_{ij}^2r_{ij}}\,. \tag{2.78}$$

The equation is a series expansion in powers of $\frac{w_{ij}r_{ij}}{c} \ll 1$. The parameter r_{ij} is inter-electron distance; therefore, $\frac{1}{r_{ij}}$ is the coulomb interaction, $\frac{\alpha_i.\alpha_j}{r_{ij}}$ is magnetic interaction and the others are a set that is a representative of the retardation operator.

2.5 Random Phase Approximation – RPA

A major transformation occurred in quantum many-body theory in the 1950s [**43**]. In 1951–1953 papers were published by **Bohm** and **Pines** introducing a technique to make the many-body more tractable by ignoring terms that nearly cancel [**43**]. The first paper they published explains this main idea, as stated in the following paragraph from that paper [**43**]:

We distinguish between two kinds of response of the electrons to a wave. One of these is in phase with the wave, so that the phase difference between the particle response and the wave producing it is independent of the position of the particle. This is the response which contributes to the organized behavior of the system. The other response has a phase difference with the wave producing it which depends on the position of the particle. Because of the general random location of the particles, this second response tends to average out to zero when we consider a large number of electrons, and we shall neglect the contributions arising from this. This procedure we call the random phase approximation.

The calculation is long and complicated and has been done in different ways. The following is a brief outline of one approach for an N-electron atom that begins by adding and subtracting a term to the Hamiltonian [**22, 31**]

$$\mathrm{H} = H_1 + H_2, \qquad \mathrm{H} = \sum_{i=1}^{N} f(r_i) + \frac{1}{2}\sum_{j=1, j\neq i}^{N}\sum_{j=1}^{N} V(r_i, r_j), \tag{2.79}$$

$$\mathrm{H} = \sum_{i=1}^{N} f(r_i) + \frac{1}{2}\sum_{j=1, j\neq i}^{N}\sum_{j=1}^{N} V(r_i, r_j) + \sum_{i=1}^{N} F(r_i) - \sum_{i=1}^{N} F(r_i), \tag{2.80}$$

where r_i represents the coordinates. Now the Hamiltonian is a summation of two parts

$$\mathrm{H} = H_0 + H', \qquad F = \sum_{i=1}^{N} F(r_i), \tag{2.81}$$

$$H_0 = \sum_{i=1}^{N} f(r_i) + \sum_{i=1}^{N} F(r_i)\,, \qquad H^{'} = \frac{1}{2}\sum_{j=1, j\neq i}^{N}\sum_{j=1}^{N} V(r_i, r_j) - \sum_{i=1}^{N} F(r_i). \qquad (2.82)$$

F is chosen so that the magnitude of $H^{'}$ becomes small and can be treated as a perturbation. Therefore, the modified Hamiltonian includes two terms: the one-electron operator H_0, plus second operator $H^{'}$ which is interaction between pairs of electrons [**31**]. Considering spin [**31**]

$$[f(\vec{r}) + F(\vec{r})]\psi_{i\sigma}(\vec{r}) = \varepsilon_j \psi_{i\sigma}(\vec{r}), \qquad (2.83)$$

where σ specifies the spin

$$\psi_{i\sigma}(\vec{r}) = \psi_{i\downarrow}(\vec{r}) \quad \text{or} \quad \psi_{i\sigma}(\vec{r}) = \psi_{i\uparrow}(\vec{r}), \qquad (2.84)$$

then by neglecting $H^{'}$, the unperturbed ground state wavefunction is [**31**]

$$\phi^{(N)} = \frac{1}{\sqrt{N!}}\begin{vmatrix} \psi_{1\uparrow}(1) & & \psi_{1\uparrow}(N) \\ \psi_{1\downarrow}(1) & & \psi_{1\downarrow}(N) \\ & \psi_{i\uparrow}(j) & \\ & \psi_{i\downarrow}(j) & \\ \psi_{\frac{N}{2}\uparrow}(1) & & \psi_{\frac{N}{2}\uparrow}(N) \\ \psi_{\frac{N}{2}\downarrow}(1) & & \psi_{\frac{N}{2}\downarrow}(N) \end{vmatrix}, \qquad (2.85)$$

$\frac{N}{2}$ at the end of columns indicates a square matrix, and after some steps

$$\left\langle \Phi_q^{(N)} \middle| F \middle| \Phi_p^{(N)} \right\rangle = \sum_{i=1}^{N} [\langle iq|V|ip\rangle - \langle qi|V|ip\rangle]. \qquad (2.86)$$

$\Phi_p^{(N)}$ and $\Phi_q^{(N)}$ represent unperturbed wave functions. The first function indicates the ground state and the second shows excited state. The approximation is based on changing the situation of only one electron in excitation from ϕ_p to ϕ_q, thus, the other single-electron orbitals remain unchanged. Then,

$$\langle \Phi^N|H|\Phi^N\rangle = E(N) = \sum_{i=1}^{N}\langle i|f|i\rangle + \sum_{j=1}^{N}\sum_{i=1}^{N}[\langle ij|V|ij\rangle - \langle ji|V|ij\rangle], \qquad (2.87)$$

where $\langle ij|V|ij\rangle$ is the electron-electron Coulomb repulsion, and electron-electron exchange interaction is given by $\langle ji|V|ij\rangle$ [**31**]. The assumption is now made that the system behaves like an electron gas of a uniform charge density [**31**], and it is known also as homogeneous electron gas (HEG) [**44**].

By the assumption of a free electron gas, an attractive potential, *F*, and electron-electron coulomb repulsion are taken to approximate cancel while the exchange interaction remains [**31**]. Pursuing the process using a screened coulomb potential V^{sc} in the second part of the Eq. (2.9) and transferring to $\vec{k}$ space (wave vector), that is applied to the replacement of $\vec{k}_1\sigma_1$, $\vec{k}_2\sigma_2$, $\vec{k}_3\sigma_3$ and $\vec{k}_4\sigma_4$ (the summation over spin variables) instead of coordinates i, j, k and l, after considerable amount of algebra, the following equation is obtained [**31, 45**]

$$\mathrm{H} = \sum_{\vec{k}_1}\sum_{\sigma_1}\sum_{\vec{k}_2}\sum_{\sigma_2} c^{\dagger}_{\vec{k}_1\sigma_1}\left\langle \vec{k}_1\sigma_1\left|\frac{P^2}{2m}\right|\vec{k}_2\sigma_2\right\rangle c_{\vec{k}_2\sigma_2}$$

$$+\frac{1}{2}\sum_{\vec{k}_1}\sum_{\sigma_1}\sum_{\vec{k}_2}\sum_{\sigma_2}\sum_{\vec{k}_3}\sum_{\sigma_3}\sum_{\vec{k}_4}\sum_{\sigma_4} c^{\dagger}_{\vec{k}_1\sigma_1}c^{\dagger}_{\vec{k}_2\sigma_2}\langle \vec{k}_1\sigma_1\vec{k}_2\sigma_2|V^{sc}|\vec{k}_3\sigma_3\vec{k}_4\sigma_4\rangle c_{\vec{k}_3\sigma_3}\, c_{\vec{k}_4\sigma_4}. \qquad (2.88)$$

where c and $c^{\dagger}$ are annihilation and creation operators, respectively. Deviation in uniform distribution of electrons inside a matter destroys neutralization of electric charge, so screened coulomb potential (V^{sc}) appears by displacement of electron gas [**44**], and then there will be a net charge at the surface of electron gas. Eq. (2.88) illustrates only a pair electron interaction, $\vec{k}_1$and $\vec{k}_2$ come with creation operators, and $\vec{k}_3$and $\vec{k}_4$ with destruction operators.

Conservation of momentum is represented by [**31**]

$$\vec{k}_1 + \vec{k}_2 = \vec{k}_3 + \vec{k}_4$$

so that, defining $\vec{q}$ as the transferred momentum,

$$\vec{k}_4 - \vec{k}_2 = \vec{k}_1 - \vec{k}_3 = \vec{q} \text{ and } \vec{k}_4 = \vec{p} \rightarrow \vec{k}_2 = \vec{k}_4 - \vec{q} = \vec{p} - \vec{q}. \quad (2.89)$$

After significant calculation it results the energy and Hamiltonian for electron gas in a certain volume that is under effect of uniform positive jellium potential [**31, 45**].

$$E_{HF}^{\substack{electron\ gas\ in \\ jellium\ potential}} = E_{\substack{kinetic \\ energy}} + E_{\substack{exchange, \\ energy}} \quad (2.90)$$

$$\mathrm{H} = \sum_{\vec{k}} \sum_{\sigma} \frac{\hbar^2 \vec{k}^2}{2m} c^{\dagger}_{\vec{k}\sigma} c_{\vec{k}\sigma} + \frac{1}{2}\frac{e^2}{V} \sum_{\vec{k},\sigma_1} \sum_{\vec{p},\sigma_2} \sum_{q \neq 0} \left[\frac{4\pi}{q^2} c^{\dagger}_{\vec{k}+\vec{q}\sigma_1} c^{\dagger}_{\vec{p}-\vec{q}\sigma_2} c_{\vec{p}\sigma_2} c_{\vec{k}\sigma_1} \right], \quad (2.91)$$

where $c^{\dagger}$ is a creation operator and c is an annihilation operator, V is the volume, e is the electron charge, and m is the mass of electron. The potential energy of the i^{th} electron because of interaction with the whole electron gas [**46**]

$$P(\vec{r}_i) = \sum_{\substack{i=1 \\ j \neq i}}^{N} \frac{e^2}{r_{ij}} = \frac{1}{V} \sum_{\substack{i=1 \\ j \neq i}}^{N} \sum_{\vec{k}}^{N} c_k \, e^{i\vec{k}\cdot(\vec{r}_i - \vec{r}_j)}. \quad (2.92)$$

On the other hand, the charge density is found simply by the equation $\rho = \frac{Ne}{V}$, and in $\vec{k}$ space [**31, 47**]

$$\rho_{\vec{k}} = \int\int\int d^3\vec{r}\, \rho(\vec{r}) e^{-i\vec{k}.\vec{r}} \;\leftrightarrow\; \rho(\vec{r}) = \frac{1}{V} \sum_{\vec{k}=1}^{N} \rho_{\vec{k}} e^{i\vec{k}.\vec{r}}. \quad (2.93)$$

To continue the procedure, we get the equation of motion for density fluctuations

$$\ddot{\rho}_{\vec{k}} = -\frac{1}{V} \sum_{\vec{k}=1}^{N} \left(\vec{k}\cdot\vec{r}_i\right)^2 e^{-i\vec{k}.\vec{r}} - \frac{1}{V}\frac{4\pi N e^2}{m} \rho_{\vec{k}} - \frac{4\pi e^2}{mV} \sum_{\substack{\vec{k}' \neq \vec{k} \\ \vec{k}' \neq 0}}^{N} \frac{\vec{k}\cdot\vec{k}'}{\left|\vec{k}'\right|^2} \rho_{\vec{k}'}\, \rho_{\vec{k}-\vec{k}'}. \quad (2.94)$$

The density fluctuations $\ddot{\rho}_{\vec{k}}$ is a summation of three parts. The third one is the quadratic term and the product of two charge densities ($\rho_{\vec{k}'}$) and ($\rho_{\vec{k}-\vec{k}'}$) that are complex exponential function

$$\rho_{\vec{k}} = \sum_{i=1}^{N} e^{-i\vec{k}\cdot\vec{r}_i} \;; \quad \rho_{\vec{k}-\vec{k}'} = \sum_{i=1}^{N} e^{i(\vec{k}'-\vec{k})\cdot\vec{r}_i}. \quad (2.95)$$

Now what is observed is a number of vectors in the complex plane that are in random directions that they approximately cancel out and the sum will be close to zero. Therefore, compared to the linear terms, the quadratic term in density fluctuations is neglected and the method is called the Random Phase Approximation [**31, 47**].

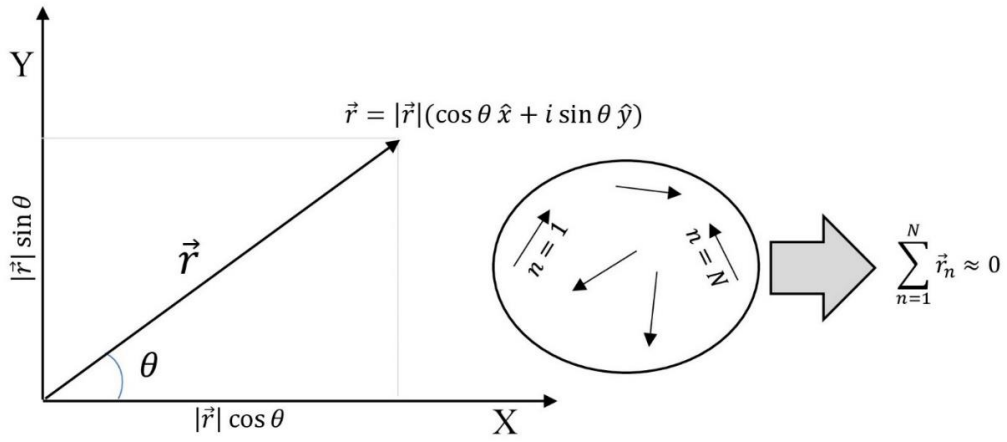

Figure 2.2: Complex plane, vectors with random directions in this plane cancel out each other.

2.6 Relativistic Random Phase Approximation – RRPA

Upgrading RPA to include relativistic effects leads to the relativistic-random-phase approximation (RRPA) methodology, which can be obtained from linearized time-dependent Dirac-Fock theory [**48**]. RRPA has been used extensively in the calculation of atomic photoionization cross sections [**49**]. Going from RPA to RRPA changes the results of calculations, owing to the extra physical interactions that relativity induces [**22**].

RRPA can be derived by linearizing the time-dependent Dirac-Fock equations (TDDF). We consider a closed-shell atom with N-electrons is in a time-dependent external field. Based on the Dirac equation [**24**]

$$(h_o + V)u_i = \epsilon_i u_i, \quad i = 1, 2, \ldots, N\,. \tag{2.96}$$

Here, the Dirac Hamiltonian for a single-electron is $h_0 = \vec{\alpha}.\vec{\mathrm{p}} + \beta m - Ze^2/r$ and ϵ_i determines the orbital eigenvalue. Note that natural units are employed ($\hbar = c = 1$). In Eq. (2.96) the DF potential $V(\vec{r})$ is represented by

$$Vu(\vec{r}) = \sum_{j=1}^{N} e^2 \int \frac{d^3r'}{|\vec{r} - \vec{r}'|}\left[(u_j^\dagger u_j)' u - (u_j^\dagger u)' u_j\right], \tag{2.97}$$

in each of the DF orbitals $u_i(\vec{r})$, a time-dependent perturbation is induced by an external field, represented by $(v_+ e^{-i\omega t} + v_- e^{i\omega t})$, so that

$$u_i(\vec{r}) \;\rightarrow\; u_i(\vec{r}) + w_{i+}(\vec{r})e^{-i\omega t} + w_{i-}(\vec{r})e^{i\omega t} + \ldots\ldots, \tag{2.98}$$

after expanding the TDDF equations in powers of the external field, only the first-order terms are retained; then for the orbitals $w_{i\pm}(\vec{r})$ the result is a set of linearized TDDF equations.

$$(h_o + V - \epsilon_i \mp \omega)w_{i\pm} = (v_\pm - V_\pm^{(1)})u_i + \sum_j \lambda_{ij\pm} u_j\,, \qquad i = 1, 2, \ldots., N, \tag{2.99}$$

where V, in Eq. (2.99) represents the DF potential [**24**]

$$V_\pm^{(1)} u_i(\vec{r}) = \sum_{j=1}^{N} e^2 \int \frac{d^3r'}{|\vec{r} - \vec{r}'|}\left[(u_j^\dagger w_{j\pm})' u_i + (w_{j\mp}^\dagger u_j)' u_i - (w_{j\mp}^\dagger u_i)' u_j - (u_j^\dagger u_i)' w_{j\pm}\right]. \tag{2.100}$$

The orthogonality of the perturbed orbitals $w_{j\pm}(\vec{r})$ to the occupied orbitals $u_i(\vec{r})$ is assured by the use of Lagrange multipliers $\lambda_{ij\pm}$. To derive the fundamental RRPA equations the "driving" terms $v_\pm$ are omitted from Eq. (2.99), which leads to the eigenvalue equation

$$\pm(h_o + V - \epsilon_i)w_{i\pm} \pm V_\pm^{(1)} u_i \mp \sum_j \lambda_{ij\pm} u_j = \omega w_{i\pm}. \tag{2.101}$$

All solutions of Eq. (2.99) can be expanded based on a complete set of solutions to the homogeneous Eqs. (2.101). This fact leads us to express the amplitude for a transition from the ground state to the excited state by $w_{i\pm}(\vec{r})$, the RRPA function of frequency ω, induced by a time-dependent external field $v_+ e^{-i\omega t} + v_- e^{i\omega t}$ (considering the frequency ω), so we have [**24**]

$$T = \sum_{i=1}^{N} \int d^3r \, (w_{i+}^{\dagger} v_{+} u_i + w_{i-}^{\dagger} v_{-} u_i). \tag{2.102}$$

2.7 Cross section and angular distribution asymmetry parameter

As mentioned in the introduction, calculating cross sections and angular distribution asymmetry parameters are the main purposes of this work. The differential photoionization cross section in the dipole approximation for a subshell $n\kappa$ by incoming unpolarized photons is [**21**]

$$\frac{d\sigma_{n\kappa}}{d\Omega} = \frac{\sigma_{n\kappa}(\omega)}{4\pi}\left[1 - \frac{1}{2}\beta_{n\kappa}(\omega) p_2(\cos\theta)\right], \tag{2.103}$$

where θ is the angle between photon and photoelectron directions and P_2 is the Legendre polynomial. κ is defined as $\kappa = \mp\left(j + \frac{1}{2}\right)$ for $j = l \pm \frac{1}{2}$, while j and l are the total and orbital momentum quantum numbers, so that the total subshell cross section $\sigma_{n\kappa}$ is [**21, 50**]

$$\sigma_{n\kappa} = \frac{4\pi^2 \alpha \omega}{3}\left(\left|D_{nj\to j-1}\right|^2 + \left|D_{nj\to j}\right|^2 + \left|D_{nj\to j+1}\right|^2\right), \tag{2.104}$$

where ω is the photon energy and $D_{nj\to j'}$ represents the reduced dipole matrix element for the channel $nj \to j'$ [**20, 21**], α is the fine-structure constant ($\alpha = \frac{e^2}{\hbar c}$), which becomes $\alpha = \frac{1}{C}$ in atomic units, i.e., $e = m_e = \hbar = 1$ [**51**]. The general formula for angular distribution asymmetry parameter β is [**20**]

$$\beta_{n\kappa}(\omega) = \begin{bmatrix} \frac{(2j-3)}{2(2j)}\left|D_{j\to j-1}\right|^2 - \frac{(2j-1)(2j+3)}{(2j)(2j+2)}\left|D_{j\to j}\right|^2 \\ + \frac{(2j+5)}{2(2j+2)}\left|D_{j\to j+1}\right|^2 \\ -\frac{3}{2j}\left(\frac{(2j-1)}{2(2j+2)}\right)^{\frac{1}{2}}\left(D_{j\to j-1}D_{j\to j}^{*} + c.c.\right) \\ -\frac{3}{2}\left(\frac{(2j-1)(2j+3)}{(2j)(2j+2)}\right)^{\frac{1}{2}}\left(D_{j\to j-1}D_{j\to j+1}^{*} + c.c.\right) \\ -\frac{3}{(2j+2)}\left(\frac{(2j+3)}{2(2j)}\right)^{\frac{1}{2}}\left(D_{j\to j}D_{j\to j+1}^{*} + c.c.\right) \end{bmatrix} \times \left[\left|D_{j\to j-1}\right|^2 + \left|D_{j\to j}\right|^2 + \left|D_{j\to j+1}\right|^2\right]^{-1},$$

(2.105)

As a special case, for ns subshells where the only allowed dipole transitions $ns \longrightarrow \varepsilon p_{\frac{1}{2}}, \varepsilon p_{\frac{3}{2}}$ the asymmetry parameter β reduces to

$$\beta = \frac{2R_{3/2}^2 + 4R_{1/2}R_{3/2}\cos(\delta_{1/2} - \delta_{3/2})}{R_{1/2}^2 + 2R_{3/2}^2}, \tag{2.106}$$

where the magnitude of the radial dipole matrix elements to the εp_j final states are given by R_j and the phase shifts denoted by δ_j. When the spin-orbit interaction is small, then $\delta_{1/2} \approx \delta_{3/2}$, and the cosine term is approximately equal to one. Now when the R_j's are approximately equal, then $\beta \approx 2$, as it is in the nonrelativistic case. In addition, when $R_{3/2} = 0$ then $\beta = 0$ and for $R_{1/2} = 0$ then $\beta = 1$. And, when the signs of two matrix elements are different and the ratio of $R_{1/2}$ to $R_{3/2}$ is -2, then Eq. (2.106) shows that $\beta = -1$ [**52**].

Atomic photoionization cross sections display a ubiquitous feature, Cooper minima, in the $l \longrightarrow l + 1$ channels outer and near-outer subshells; this has been found both theoretically and experimentally [**53**]. A Cooper minimum occurs where the negative and positive contributions of a dipole matrix element cancel so that the matrix element goes to zero and changes sign [**52, 53**]. It is a very delicate balance and, comparison with experiment in the region of a Cooper minimum provides an excellent test of theory.

There are alternative forms for the dipole transition operator and matrix elements. Starting with Eq. (2.1) and the vector potential (Eq. 2.3), we obtain H_{int} (Eq. 2.5). The matrix elements of the momentum operator in H_{int} can be written in terms of a commutation relation [**54**]

$$\sum_{i=1}^{N} P_i = -i\left[\sum_{i=1}^{N} r_i, H\right], \tag{2.107}$$

and

$$\left[\sum_{i=1}^{N} r_i, H\right] = -i\sum_{i=1}^{N} \frac{Zr_i}{r_i^3}. \tag{2.108}$$

The energies of eigenstates ψ_0 and ψ_f are E_0 and E_f, respectively, and the difference between these two is $\omega = E_f - E_0$, so that

$$\langle\psi_0|\sum_{i=1}^{N} P_i\,|\psi_f\rangle = -i\omega\langle\psi_0|\sum_{i=1}^{N} r_i\,|\psi_f\rangle\,, \tag{2.109}$$

$$\langle\psi_0|\sum_{i=1}^{N} P_i\,|\psi_f\rangle = -\frac{i}{\omega}\left\langle\psi_0\left|\sum_{i=1}^{N}\frac{Zr_i}{r_i^3}\right|\psi_f\right\rangle. \tag{2.110}$$

where three alternative forms of the dipole matrix element that were given above are $\sum_{i=1}^{N} P_i$, $\sum_{i=1}^{N} r_i$ and $\sum_{i=1}^{N}\frac{Zr_i}{r_i^3}$, and yield the "velocity", "length" and "acceleration" forms (or gauges) of the dipole matrix elements, respectively. With exact wave functions, the results using each of these forms are equal, and the same is true in RRPA. Thus, all calculations have been done in both length and velocity gauges as a check on numerical accuracy.

2.8 Confined atom in a quantum well

Atoms confined in a potential well are also of interest. A good example is a fullerene molecule that makes a hollow cage that can act as a quantum well [**55**]. The best known fullerene is C_{60}, which encage an atom in C_{60} alters its properties [**56**].

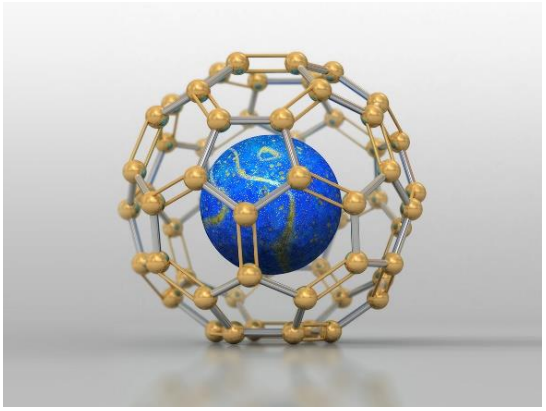

Figure 2.3: An atom inside the cage [**57**].

The nearly spherical shape is the reason for the selection of C_{60}, because the calculations are dramatically simplified by approximating the actual C_{60} potential by a finite spherical well, a

symmetric potential, $V_c(r)$, with dimensions, inner radius r_{in} = 5.8 au, width of the confining potential Δ = 1.9 au and the depth of the confining potential V_0 = 0.302 au [**58**], i.e.,

$$V_c(r) = -V_0 \quad \text{in the range} \quad r_{in} \le r \le r_{in} + \Delta, \text{otherwise,} \quad V_c(r) = 0.$$

When an atom is trapped inside of a hollow fullerene cage, this is known as an endohedral fullerene, and is depicted in Figure 2.3. Studies of endohedrally confined atoms have shown strong resonances in the photoionization cross sections that are called confinement resonances [**58**] and these are discussed below. In this work, copernicium was selected as an example to display the effects of confinement on the photoionization parameters.

3 CALCULATION METHODOLOGY

The calculation begins with using the Dirac-Fock (DF) [**59**], methodology to obtain discrete wave functions and subshell threshold energies to use as input into the photoionization calculation. The removal of the nonrelativistic degeneracy between nl states with $l + s$ and $l - s$ under effect of relativity begins by replacing the one-electron Schrödinger orbital $\psi(\vec{r})$ with corresponding Dirac orbital $\varphi(\vec{r})$ [**51**].

$$h_D\varphi(\vec{r}) = E\varphi(\vec{r}), \tag{3.1}$$

where h_D is the Dirac Hamiltonian, and in atomic units is given by

$$h_D = c\vec{\alpha}.\vec{\mathrm{p}} + \beta c^2 + V(r). \tag{3.2}$$

Dirac equation has been discussed in section (2.3). Here the radial potential has been added in Eq. (3.2). α and β were introduced in Eqs. (2.25 & 2.26), and the speed of light is equal to c = 137.0359895… in atomic units. Regarding two-component representation of $\vec{S}$, the eigenstates of h_D could be classified based on the eigenvalues of energy, j^2 and j_z. Thus, the spherical spinors ($\Omega_{\kappa m}(\hat{r})$) as the eigenstates of j^2 and j_z is constructed [**51**].

$$\varphi_\kappa(\vec{r}) = \frac{1}{r}\begin{pmatrix} iP_\kappa(r) & \Omega_{\kappa m}(\hat{r}) \\ Q_\kappa(r) & \Omega_{-\kappa m}(\hat{r}) \end{pmatrix}. \tag{3.3}$$

At the first step, P_κ and Q_κ are defined in a special case $V(r) = {-Z}/{r}$ by two differential equations for large r; only the dominant terms are retained as $r \to \infty$,

$$c\frac{dQ_\kappa}{dr} = (E - c^2)P_\kappa, \tag{3.4}$$

$$c\frac{dP_\kappa}{dr} = -(E + c^2)Q_\kappa, \tag{3.5}$$

we may convert them into a second-order equation

$$c^2\frac{d^2P_\kappa}{dr^2} + (E^2 - c^4)P_\kappa = 0. \tag{3.6}$$

$e^{-\lambda r}$ represents two linearly independent solutions, which $\lambda = \sqrt{c^2 - {E^2}/{c^2}}$, then acceptable solutions are as follows

$$P_\kappa(r) = e^{-\lambda r}, \quad \text{and} \qquad Q_\kappa(r) = \sqrt{\frac{c^2 - E}{c^2 + E}}e^{-\lambda r}, \tag{3.7}$$

in atomic units $c = {1}/{\alpha}$ and introducing the parameter, $\gamma = \sqrt{\kappa^2 - \alpha^2 Z^2}$, finally the eigenvalue equation (E) for an atom with atomic number Z is

$$E_{n\kappa} = \frac{c^2}{\sqrt{1 + \dfrac{\alpha^2 Z^2}{(\gamma + n - k)}}}, \tag{3.8}$$

where $k = |\kappa|$ and κ was defined in section **2.7**, so n as the principal quantum number specifies the number of eigenfunctions for negative ($\kappa = -1, -2, \ldots, -n$) and $n - 1$ eigenfunctions for positive ($\kappa = 1, 2, \ldots, n - 1$). Eq. (3.6) may be expanded by the power of αZ

$$E_{n\kappa} = c^2 - \frac{Z^2}{2n^2} - \frac{\alpha^2 Z^4}{2n^3}\left(\frac{1}{k} - \frac{3}{4n}\right) + \cdots. \tag{3.9}$$

Electron's rest energy (mc^2) is displayed as the first term by c^2 because of atomic units. The second is simply the nonrelativistic Coulomb-field binding energy. Fine-structure correction

appears as the third term, for example by this formula the energy difference between $2p_{3/2}$ and $2p_{1/2}$ levels in Hydrogen atom is calculated as following [**51**]

$$\Delta E_{2p} = \frac{\alpha^2}{32}\, au = 0.3652\ cm^{-1}. \tag{3.10}$$

Eq. (3.9) obviously shows degeneracy of energy between $l + s$ and $l - s$. Generally, this method is used for an atom with independent electrons, but in real atom correlation changes the condition. Therefore, finding the binding energies of the subshells of an atom with high Z number of electrons requires considering some extra terms in Hamiltonian and new wave function. Remembering Eqs. (2.54&2.75), and by the pre-assumption of $\varphi_a(\vec{r}_1)\varphi_b(\vec{r}_2)\ldots\varphi_n(\vec{r}_N)$ is the eigenfunction of H_0 with eigenvalue $E^0_{ab\ldots n} = \epsilon_a + \epsilon_b + \cdots + \epsilon_n$, then we have a Slater determinant which is considered as an antisymmetrized wave function which is formed with new notation (**52**).

$$\Psi_{ab\ldots n}(\vec{r}_1, \vec{r}_2, \ldots, \vec{r}_N) = \frac{1}{\sqrt{N!}}\begin{vmatrix} \varphi_a(\vec{r}_1) & \varphi_b(\vec{r}_1) & \ldots\ldots & \varphi_n(\vec{r}_1) \\ \varphi_a(\vec{r}_2) & \ldots\ldots\ldots & \ldots\ldots & \ldots\ldots \\ \ldots\ldots & \ldots\ldots\ldots & \ldots\ldots & \ldots\ldots \\ \varphi_a(\vec{r}_N) & \varphi_b(\vec{r}_N) & \ldots\ldots & \varphi_n(\vec{r}_N) \end{vmatrix}, \tag{3.11}$$

it contains N lowest-energy single-particle orbitals for the ground-state of a closed-shell atom, then we obtain (**51**)

$$E_{ab\ldots n} = \sum_a \langle a|h_0|a\rangle + \frac{1}{2}\sum_{ab}(g_{abab} - g_{abba}). \tag{3.12}$$

This is the same as nonrelativistic case, which is discussed in previous sections, but here we use Dirac orbitals rather than nonrelativistic orbitals to evaluate the Coulomb matrix elements (g_{abcd}). Coulomb interaction g (r_{12}) = $\frac{1}{r_{12}}$ is described by two matrix elements g_{abab} and g_{abba}. The first is named the direct matrix element of the operator g (r_{12}) while the second is the exchange matrix element.

In terms of spherical spinors, $\Omega_{\kappa_a m_a}(\hat{r})$, the one-electron Dirac orbital is defined

$$\varphi_a(\vec{r}) = \frac{1}{r}\begin{pmatrix} P_a(r)\Omega_{\kappa_a m_a}(\hat{r}) \\ iQ_a(r)\Omega_{-\kappa_a m_a}(\hat{r}) \end{pmatrix}, \tag{3.13}$$

so that the energy, in terms of the various nl orbitals comprising the state, is given by

$$E_{ab\ldots n} = \sum_{n_a l_a} 2(2\,l_a + 1)\left\{ I(n_a l_a) + \sum_{n_b l_b}(2l_b + 1)(R_0(n_a l_a, n_b l_b, n_a l_a, n_b l_b) - \sum_{l} \Lambda_{l_a l l_b}\, R_l(n_a l_a, n_b l_b, n_a l_a, n_b l_b))\}\right\}, \tag{3.14}$$

where

$$I(n_a l_a) = \int_0^\infty dr \left[\frac{1}{2}\left(\frac{dP_{n_a l_a}}{dr}\right)^2 + \frac{l_a(l_a+1)}{2r^2} P_{n_a l_a}^2 - \frac{Z}{r} P_{n_a l_a}^2\right], \tag{3.15}$$

and

$$a_{JLM} = \int_0^{2\pi} d\phi \int_0^{\pi} \sin\theta\, d\theta Y_{JLM}^{\dagger} \vec{r} Y_{lm}(\theta, \phi), \tag{3.16}$$

and $\Lambda = 2\vec{\mathrm{L}}\cdot\vec{\mathrm{S}} = 2l_z S_z + L_+ S_- + L_- S_+$,

$$\Lambda_{l_a l l_b} = \frac{\langle l_a || C^l || l_b\rangle^2}{2(2l_a+1)(2l_b+1)} = \frac{1}{2}\begin{pmatrix} l_a & l & l_b \\ 0 & 0 & 0 \end{pmatrix}, \tag{3.17}$$

where Wigner three-j symbols $\begin{pmatrix} j_1 & j_2 & j_3 \\ m_1 & m_2 & m_3 \end{pmatrix}$ displays the symmetry relations between the Clebsch-Gordan coefficients (**51**)

$$\begin{pmatrix} j_1 & j_2 & j_3 \\ m_1 & m_2 & m_3 \end{pmatrix} = \frac{(-1)^{j_1 - j_2 - m_3}}{\sqrt{2j^3+1}} C(j_1, j_2, j_3; m_1, m_2, -m_3), \tag{3.18}$$

then

$$\langle l_a || C^l || l_b\rangle = (-1)^{l_a}\sqrt{(2l_a+1)(2l_b+1)}\begin{pmatrix} l_a & l & l_b \\ 0 & 0 & 0 \end{pmatrix}. \tag{3.19}$$

The relativistic-random-phase approximation (RRPA) [**24**] is used to calculate the photoionization cross sections. Since it is based on the Dirac equation, RRPA includes relativity

in an *ab initio* manner. RRPA also includes significant aspects of correlation such as two-particle two-hole pair excitation correlations in the initial state and interchannel coupling (essentially configuration interaction) in the final continuum state. An important aspect of the RRPA methodology is that it allows us to perform truncated calculations; it allows us to control which photoionization channels are included. Performing such calculations spotlights which specific aspects of interchannel coupling are the crucial ones in any particular case. Another important aspect of the RRPA calculation is that the photoionization calculations when all channels are included and Dirac–Fock (DF) [**38**] energies are used are gauge-invariant, i.e., length and velocity formulations must be equal. This equality is preserved to a substantial extent even in truncated RRPA and serves as a check on the numerical methodology.

In order to be able to understand the shape of the various photoionization parameters, as functions of the photon energy, a very file mesh of energy points was required in the calculations. We, thus, used a mesh of 0.01 au generally; in the few places where this mesh was still not fine enough to display the results, an energy mesh of 0.002 au was used.

In addition, below each threshold are infinite number of resonances. For example, below a 6*s* ionization threshold are the discrete (autoionizing) excitations, $6s \rightarrow np$ and $6s \rightarrow np^*$. These resonances occur in a small region, something like 0.1 - 0.2 au below each threshold, and the shapes of the resonances are complicated. In addition, from a numerical point of view, convergence of the RRPA methodology is difficult in the resonance regions. Since we were interested in the broad overall characteristics of the photoionization region, these small autoionizing regions below each threshold were omitted in our plots.

Since the DF energies and wave functions are input to the RRPA calculations, we include the presentation and discussion of the DF results in the present section. The bound-state DF

calculations start with the one-electron Dirac Hamiltonian for each electron plus the Coulomb interactions between the electrons. The DF wave function is an antisymmetrized product of one-electron Dirac orbitals (including spin). The diagonal matrix element of the Hamiltonian $\langle H \rangle$ is taken with this wave function and the angular and spin parts integrated out analytically. Then, using the calculus of variations, the $\langle H \rangle$ is minimized with respect to the radial part of each orbital, with constraints on normalization and orthogonality, yielding a set of coupled integro-differential equations, the DF equations. The solution of these equations yields the radial part of each of the single-electron orbitals.

Calculating the binding energies by Schrödinger equation is based on independent particles, but the assumption in Dirac-Fock method is an atom as a system including all electrons which are correlated with each other. Thus, when one electron leaves the atom the whole system changes and there will be a new wave function of electron configurations. This is why calculating the binding energies of subshells becomes so complicated and it could be done only by numerical calculations. It is the procedure that we did in this investigation by a Fortran code. The DF calculation was performed for the three superheavy elements, No, Cn and Og. In the periodic table, Nobelium with the electron configuration, ($\{Rn\}5f^{14}7s^2$), lies below Ytterbium (Yb, Z = 70) with electron configuration ($\{Xe\}4f^{14}6s^2$). Copernicium ($\{Rn\}5f^{14}6d^{10}7s^2$) and Oganesson ($\{Rn\}5f^{14}6d^{10}7s^27p^6$) are respectively below Mercury (Hg, Z = 80, $\{Xe\}4f^{14}5d^{10}6s^2$) and Radon (Rn, Z = 86, $\{Xe\}4f^{14}5d^{10}6s^26p^6$) [**60, 61**]. The resulting energies are given in Table 3.1. No (Z = 102) is Yb-like, but with an outer-shell structure $5f^{14}7s^2$, in contrast to Yb which is $4f^{14}6s^2$. The ordering of levels is essentially exactly like the ordering in Yb, except for the increased principle quantum numbers in the outermost shells of No. Cn (Z = 112) is Hg-like, but only in a general sense; the energy levels of the subshells, seen

in Table 3.1, display several important differences. To begin with, the $5d^{10}6s^2$ outer shell structure of Hg becomes, not the $6d^{10}7s^2$ configuration, but instead, owing to relativistic interactions, $(6d_{3/2})^4(7s)^2(6d_{5/2})^6$ so that the valence level is $6d_{5/2}$. This is in agreement with the ordering found in several earlier rather sophisticated calculations [**5**], so despite the energies being close together, the DF level ordering appears to be accurate.

Table 3.1: The ground states' binding energies of the subshells for three elements (in atomic units, $1au = 27.211eV$).

Dirac-Fock and Hartree-Fock binding energies for three elements

		No, Z = 102			Cn, Z = 112			Og, Z = 118	
	subshell	relativistic	non-relativistic		relativistic	non-relativistic		relativistic	non-relativistic
1	1s	-5526.6492490	-4600.9428594	1s	-7070.7147734	-5583.7951304	1s	-8185.1346516	-6221.0302619
2	2s	-1082.8193711	-821.7823636	2s	-1444.8456191	-1016.1945642	2s	-1718.7547338	-1144.5124691
3	2p*	-1047.3646150	-797.1421253	2p*	-1405.7154919	-988.7379091	2p*	-1681.7061207	-1115.3523095
4	2p	-808.7867096	-797.1421252	2p	-1007.0985135	-988.7379091	2p	-1138.5461605	-1115.3523095
5	3s	-285.4040671	-216.8507147	3s	-390.8074553	-277.1170518	3s	-471.1806726	-318.4142207
6	3p*	-269.1039847	-204.5072768	3p*	-371.9798633	-263.0897012	3p*	-451.7237138	-303.3601947
7	3p	-212.1866551	-204.5072767	3p	-274.9938428	-263.0897011	3p	-318.3354233	-303.3601947
8	3d*	-187.1336078	-181.6835085	3d*	-245.8879634	-237.1137862	3d*	-286.6504981	-275.4568660
9	3d	-176.4436444	-181.6835085	3d	-229.4005997	-237.1137862	3d	-265.6763302	-275.4568660
10	4s	-78.6205250	-58.9875817	4s	-113.4447774	-79.8881027	4s	-140.9722153	-95.3061471
11	4p*	-70.9714669	-53.0088292	4p*	-104.2367172	-72.8968908	4p*	-131.0198217	-87.6939113
12	4p	-55.2109961	-53.0088291	4p	-76.3776203	-72.8968908	4p	-92.0240952	-87.6939113
13	4d*	-43.2369177	-41.8801011	4d*	-62.0862326	-59.8388266	4d*	-76.2652420	-73.4510418
14	4d	-40.4568692	-41.8801011	4d	-57.5617763	-59.8388266	4d	-70.3500643	-73.4510417
15	4f*	-24.6879425	-26.3038506	4f*	-38.8299502	-41.4600856	4f*	-49.7918273	-53.3659315
16	4f	-23.9145249	-26.3038506	4f	-37.5159947	-41.4600856	4f	-48.0426219	-53.3659315
17	5s	-18.8060262	-13.5523897	5s	-30.0559133	-20.4511718	5s	-39.8836639	-26.4186447
18	5p*	-15.5428171	-11.0142505	5p*	-25.8871008	-17.3161469	5p*	-35.1831409	-22.9048107
19	5p	-11.4373669	-11.0142505	5p	-17.9972913	-17.3161469	5p	-23.6625804	-22.9048107
20	5d*	-6.6105384	-6.4761070	5d*	-11.8526849	-11.6066017	5d*	-16.6629716	-16.4532444
21	5d	-5.9860040	-6.4761070	5d	-10.7070443	-11.6066017	5d	-15.0704631	-16.4532444
22	6s	-2.7953902	-1.8860046	6s	-5.6805678	-3.5633008	6s	-8.9865031	-5.7344037
23	6p*	-1.7277086	-1.1060288	6p*	-4.1231458	-2.4619152	6p*	-7.0769104	-4.3686302
24	6p	-1.0494551	-1.1060288	5f*	-3.3349698	-4.1720802	5f*	-6.5111038	-7.8669341
25	5f*	-0.5668821	-0.9635694	5f	-3.0925268	-4.1720802	5f	-6.1408301	-7.8669341
26	5f	-0.4693359	-0.9635694	6p	-2.4156562	-2.4619152	6p	-4.2163825	-4.3686302
27	7s	-0.2093299	-0.1704697	6d*	-0.5627333	-0.6961613	6d*	-1.7639234	-2.0210021
28				7s	-0.4511341	-0.2381287	6d	-1.4928989	-2.0210021
29				6d	-0.4420894	-0.6961612	7s	-1.2968896	-0.7738820
30							7p*	-0.7394454	-0.3943795
31							7p	-0.3056531	-0.3943795

In the table, nl indicates $j = l + \frac{1}{2}$; *nl* indicates* $j = l - \frac{1}{2}$

In addition, Cn displays an unusual ordering of inner shells. Specifically, Table 3.1 shows that both of the 5f thresholds lie between the $6p_{3/2}$ and the $6p_{1/2}$ levels owing to the huge relativistic spin–orbit splitting of $6p_{3/2}$ and the $6p_{1/2}$. The splitting is seen to be 1.707 a.u. (about 46.45 eV) and the 5f thresholds, which are split by only 0.242 a.u. (6.59 eV), are nestled between the 6p thresholds. The fact that the $5f_{7/2}$ threshold is 0.677 a.u. (18.42 eV) deeper than $6p_{3/2}$, while $5f_{5/2}$ lies 0.788 a.u. (21.44 eV) above $6p_{1/2}$ means that these energy separations are so large that the addition of correlation to the calculation could not change the qualitative nature of the unusual subshell ordering. For Og, which is in the noble gas column, the valence structure is normal, as seen in Table 3.1. However, the peculiar ordering of the $5f$'s, between the $6p_{3/2}$ and the $6p_{3/2}$ levels, is similar to the Cn case, with similarly large energy splittings so that this result also could not be altered qualitatively by the effects of electron–electron correlation. Also shown in the table is the comparison of relativistic and nonrelativistic energies of the various subshells of the three elements. Aside from some differences in the outer and near-outer subshell ordering between relativistic and nonrelativistic energies, it is seen for the deep inner shells, relativistic interactions increase the binding energies very significantly; as much as nearly 50 keV for the 1s subshell of Og.

4 RESULTS AND DISCUSSION

In this section, the results of the calculations of cross section and photoelectron angular-distribution asymmetry parameter, β, are presented. Experiment would provide helpful information [**62**], but this is not possible at present because of the very short half-life of the three elements under consideration [**52**]. Therefore, we have only theory using the methods which have been described in Section **2** and these methods have been confirmed for lighter elements

experimentally [**63**]. Calculations were based on RRPA method, at the level of dipole approximation, using both length and velocity formulations [**5**] as a check on the numerical calculations. And calculations, in many cases, have been performed both with all of the coupling of the relevant channels (fully coupled) and without coupling to channels from different subshells as a way of illustrating the effect(s) of interchannel coupling; in many of the figures, comparisons are shown. In each case, we scrutinize the valence (outermost) subshell in great detail as a model for all the subshells.

4.1 Nobelium (Z=102)

To begin with, we consider nobelium, No, Z=102. The calculated valence 7s cross sections and β parameter are shown in Figures 4.1 and 4.2 respectively; depicted along with the fully coupled results are the uncoupled (only the 7s channels included) for comparison this comparison allows us to understand how much the interchannel coupling contributes to the photoionization parameters, the cross section and the β parameter. Interchannel coupling phenomenology seen is a particular manifestation of a general result in photoionization; when a small cross section is degenerate with a large one, the small cross section will generally take on the characteristics of the large one owing to what amounts to configuration interaction in the final continuum state so that the wave function of the final state of the channel with the small cross section is mixed with the wave function of the channel with the large cross section, thereby leading to the transfer of oscillator strength from the large cross section to the smaller one [**19, 54, 67**]. To see this quantitatively, from a perturbation point of view, the fully coupled dipole matrix element, $D_i(E)$, of channel i can be written in terms of the uncoupled matrix elements, $M_j(E)$, of the various photoionization channels j as [**23**]

$$D_i(E) = M_i(E) + \sum_j \int dE' \frac{< \psi_i(E)|H - H_0|\psi_j(E') >}{E - E'} M_j(E'), \qquad (4.1)$$

where $H - H_0$ is the perturbing Hamiltonian, and $\psi_i(E)$ and $\psi_j(E')$ are, respectively, final continuum state wave functions of channels i and j and energies E and E'.

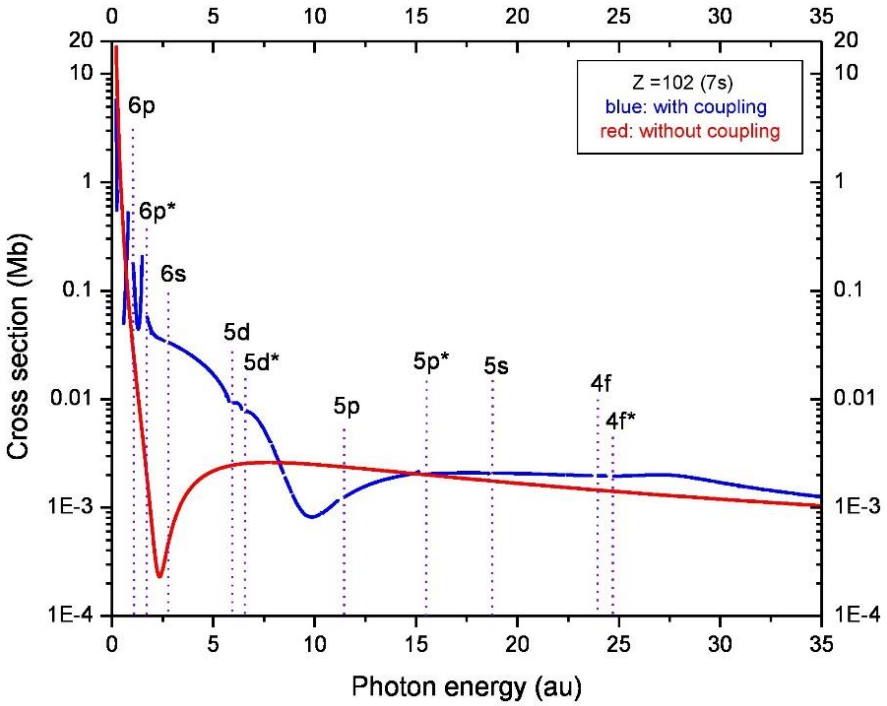

Figure 4.1: No, $7s$, cross section with and without coupling. Vertical lines indicate thresholds.

Discontinuities are seen in the fully coupled results, both cross section and β parameter, below each inner-shell threshold of about 0.1 to 0.2 au; these are the regions of the autoionizing resonances (infinite series of discrete excitations from the inner shells which undergo Auger decay) which we omit for simplicity in presenting the present results [**5**]. In what follows, we use the notation nl and nl^* as shorthand for the $j = l + \frac{1}{2}$ and $j = l - \frac{1}{2}$ components of the spin-orbit doublet, respectively.

Taking into account the characteristics of the curves, maxima and minima, there are some similarities between the cross section and angular distribution but the information that each one reveals are different.

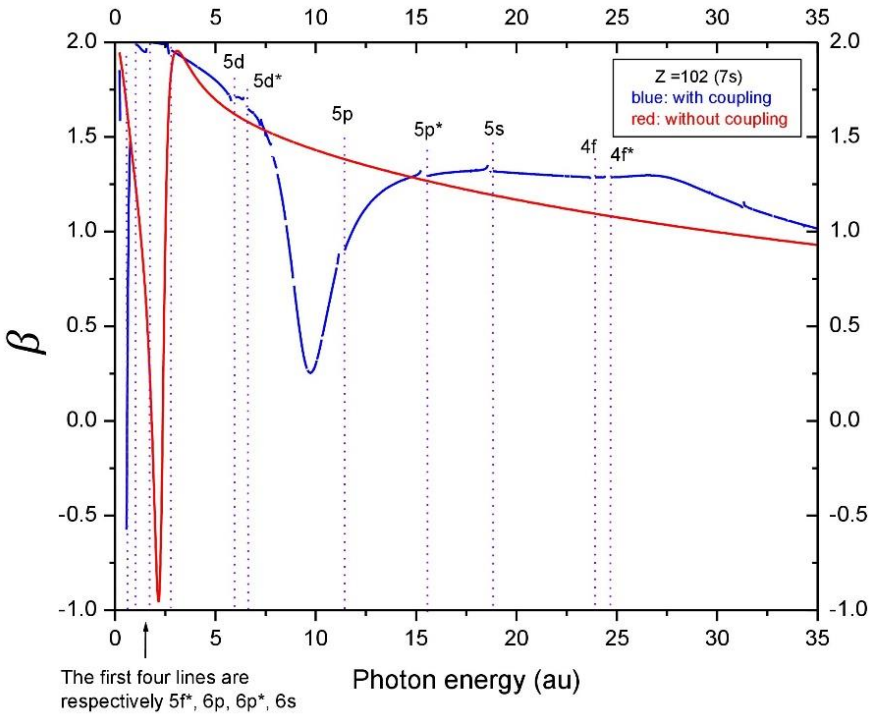

Figure 4.2: No, $7s$, β with and without coupling. Vertical lines indicate thresholds.

Looking at Figure 4.1, near threshold, the red curve (without coupling) decreases continuously with a steep slope until the minimum. Similarly, for β, Figure 4.2, but it is obvious in both, that coupling is the responsible for a significant change (from red to blue). In the interval from threshold (0.21 au) until the threshold of $7s$, the behavior of both cross section and β coupled (blue) curves are peculiar because of the high density of thresholds of the subshells in this area. In addition to deviating from a smooth path, a huge displacement of the Cooper minimum is observable that is from 2.35 to 9.89 au in Figure 4.1 for the cross section and from 2.17 to 9.73 au in Figure 4.2 for β. It is, thus clear that interchannel coupling has a huge effect on the photoionization of the 7s subshell over a large energy range.

Another interesting consequence of interchannel coupling is the small maximum in the 7s cross section and β just below 27 au. The maximum is near the thresholds of $4f$ and $4f^*$, as seen in Fig. 4.3, which shows the interchannel coupling effect of the two subshells, $4f$ and $4f^*$,

separately; the effect is coalesced into a single maximum, as seen, since the $4f$ and $4f^*$ thresholds are so close together in No.

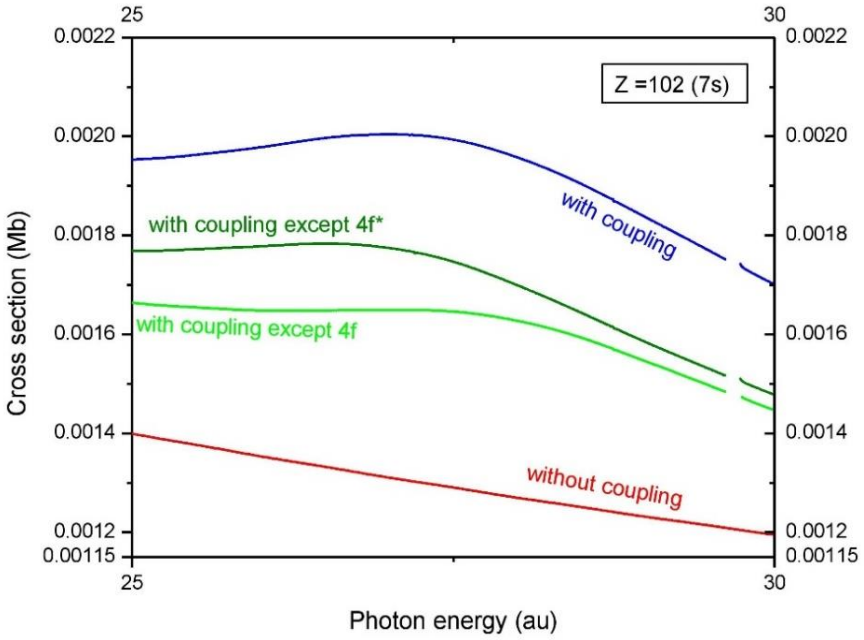

Figure 4.3: No, 7*s* cross section at various levels of coupling, as indicated.

Now all subshells do not have equal effects in regards to interchannel coupling. To investigate this idea as to which subshell or subshells dominate the interchannel coupling effects, calculations including various levels of coupling were performed, and the important subshells affecting the coupling were ascertained in each energy region. The results are given in Fig. 4.4. We emphasize that different subshells dominate the interchannel coupling in different energy regions. Basically, the subshells with the largest cross sections dominate the interchannel coupling in each energy region. Thus, from 0.21 au until 2 au, $6p$ and $6p^*$ photoionization channels dominate the coupling. Between 2 au and 12 au it is $5f$ and $5f^*$, while at the highest energies, (17 au to 35 au) the dominant effect comes from the $4f$ and $4f^*$ subshells. And in the region 12 au to 17 au both $5f$ and $5f^*$ and $4f$ and $4f^*$ are important.

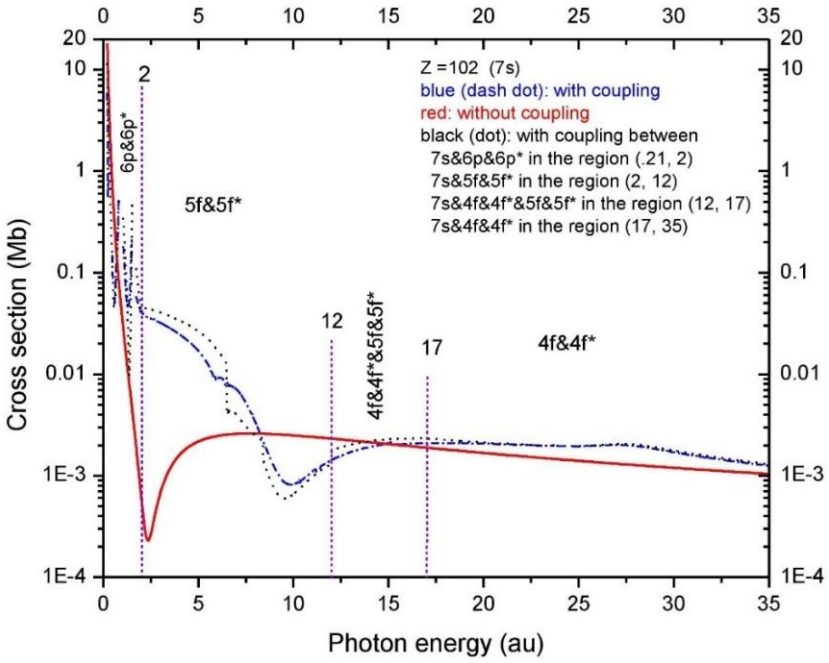

Figure 4.4: No, 7*s* cross section at various levels of coupling, as indicated.

We repeated this procedure for the photoelectron angular distribution, β, shown in Fig. 4.5, and the results, as far as what interchannel couplings are important in which energy region is quite similar to what was seen for the cross section.

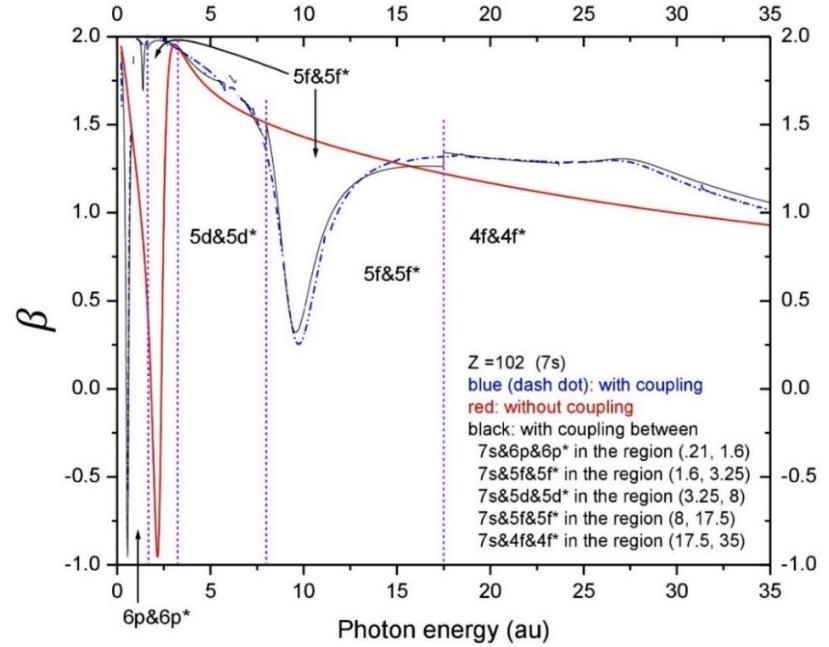

Figure 4.5: No, 7*s*, β at various levels of coupling, as indicated.

The study of the 7*s* subshell was presented in detail as an example of the importance of the interchannel coupling effects. To see the overall picture for No photoinization from threshold to 35 au, the total and subshell cross section for all open subshells in this energy region are presented in Figure 4.6 for both "with coupling" that includes the interchannel coupling among all of the relativistic single-excitation photoionization channels arising from subshells 7*s* through $4f^*$, and "without coupling" that only includes coupling among the channels from the given subshell. The closed channels, from $4d$ and below, are far enough away in energy that their omission should be of little consequence in the photon energy range considered herein; less than a 1% effect. In any case, over a significant fraction of the energy range shown, the cross section is dominated by the 5*f* subshells. At the highest energies considered, the $4f$ cross sections are seen to dominate, starting at a photon energy of about 26 au. Both the $5f$ and the $4f$ cross sections are small at their respective thresholds, owing to the huge angular momentum barrier that almost completely suppresses the $f \rightarrow g$ transitions at low photoelectron energy. The delayed maxima (shape resonances) are well-known phenomena in atomic photoionization [**66**]. The $4f$ and $4f^*$ subshells' cross sections, seen in Fig. 4.6, show this quite nicely. The subshells' cross sections are small at threshold and decreasing with energy because it is dominated by the $4f \& 4f^* \rightarrow \varepsilon g$ transitions near threshold. With increasing energy, the εg continuum wave begins to penetrate the centrifugal barrier and engenders a dramatic rise of the subshell cross section by more than an order of magnitude. And this is the behavior of all of the nf cross sections, although some of the low-energy behavior occurring in resonance regions is obscured.

The $4f$ cross sections do not include Cooper minima since the initial state wave functions are nodeless, but both $5f$ cross sections are seen to exhibit very prominent Cooper minima at around 12 au. In the region around the Cooper minima, the major contributors to the total cross

section are the $5d$ subshell cross sections along with the $5p$ cross section over part of that range. However, even the second maxima of the $5f$ cross sections, above the Cooper minima, are a significant fraction of the total cross section, even though the magnitude of the $5f$ cross section in this second maximum region is more than a factor of ten smaller than the $5f$ cross section in the shape resonance region.

Of particular interest are the relativistic and interchannel coupling effects. For example, looking at the $5p$ and $5p^*$ subshells, that are split by more than 100 eV, the cross sections, as functions of energy, are seen to be rather different; the $5p^*$ cross section drops rapidly from threshold, while for the $5p$ the falloff with energy is much more gradual. This indicates that relativistic effects on the wave functions themselves are large, and not just on the binding energies. And the 7s subshell cross section, discussed in detail above, looks rather like the $5f$ cross section, over most of the energy range, as seen in Fig. 4.6, only several orders of magnitude smaller. Nevertheless, the magnitude of the cross section is altered by as much as two orders of magnitude, owing to the interchannel coupling. Now, in Eq. 4.1, if i represents the 7s channel and the j's are the $5f$ channels, Eq. 4.1 shows that, in the regions where the $5f$ dipole matrix elements are so much larger than the 7s, the first term on the right-hand side of the equation, the zero-eth order 7s matrix element, will be much smaller than the second term, the first order perturbation. Thus, from this equation, the 7s matrix element (and the cross section) will be strongly affected by the $5f$ cross sections, but much smaller owing to the smallness of the interchannel coupling matrix element, $< \psi_i(E)|H - H_0|\psi_j(E') >$. This is *exactly* what is seen in Figure 4.4. And, although the effect is largest on the 7s cross section, it is evident from Figure 4.4 that essentially all of the smaller subshell cross sections are strongly affected by the larger ones and the explanation is the same as the above explanation for the 7s cross section.

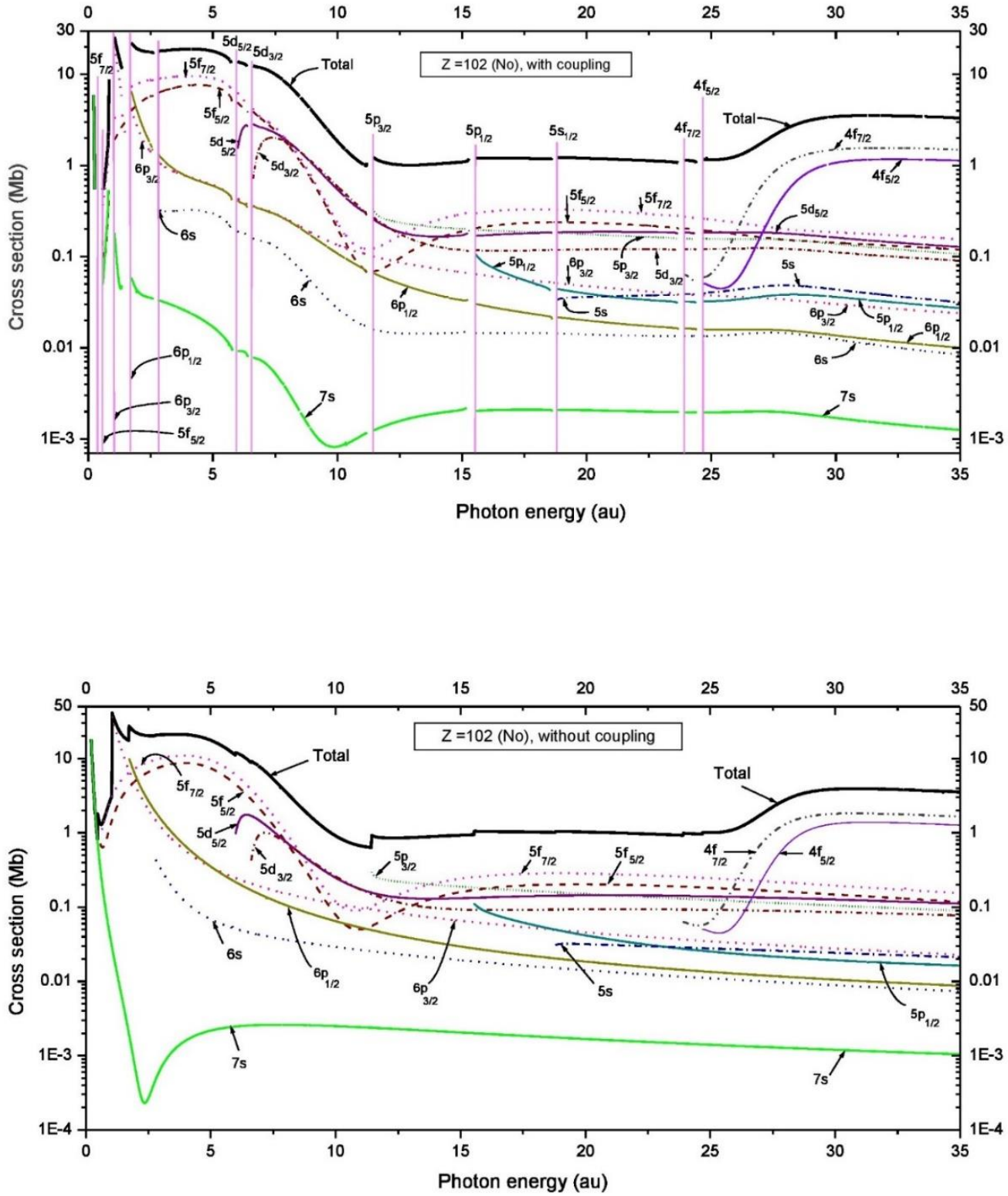

Figure 4.6: Total and subshell photoionization cross section from $7s$ to $4f^*$ for No "with coupling" (upper panel) and "without coupling" (lower panel). The vertical lines in the upper curve indicate the variuos subshell thresholds.

These ideas can be quantified by looking at the ratio of cross sections “with” vs. “without” coupling shown in Figure 4.7; note the log scale. For simplicity, only the nl cross sections are shown, not the nl^*.

Clearly 7s exhibits the greatest change and then 6s; this is because the uncoupled cross sections are so small that the matrix elements are dominated by the second (coupling) term in Eq. (4.1). Between the thresholds of $5p^*$ and $4f$ almost all ratios are parallel and near unity showing that interchannel coupling is not important here. Above the $4f$ and $4f^*$, interchannel coupling is again seen to be important and the coupling affects different subshells differently in the sense that some of the cross sections increase and others decrease under influence of coupling.

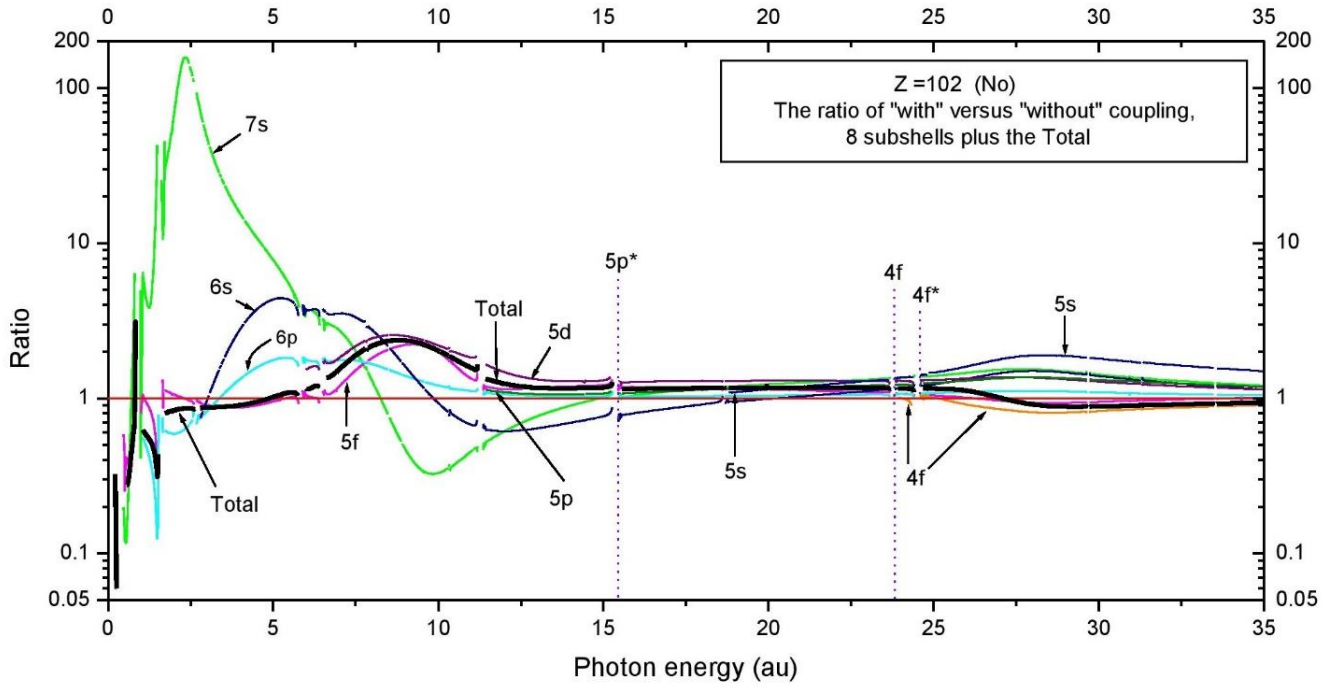

Figure 4.7: Ratio of subshell and total No photoionization cross sections “with” and “without interchannel coupling. The vertical lines indicate thresholds.

4.2 Copernicium (Z=112)

A- Free atom

Next, we consider Cn, $Z = 112$ whose valence subshell $6d$. The $6d$ cross section is presented in Figure 4.8 showing the effect of interchannel coupling by comparing "with" and "without" coupling results from threshold (0.443 au) to 50 au (1360.6 eV). In the threshold region, below about 4 au, where the $6d$ cross section dominates, there is very little in the way of interchannel coupling. At higher energies, however, the coupling completely changes the shape of the cross section. The uncoupled result has Cooper minima in the 10 au range with does not show up in the cross section; they are in the $d \rightarrow f, f^*$ channels and the $d \rightarrow p$ channel does not have a minimum, thus leading to the change of slope see in the uncoupled result. The coupled result shows two regions of minima, one at about 5 au and a second at about 15 au. Thus, the coupling changes the location and shape of the lower Cooper minima region and induces a second minimum at much higher energies.

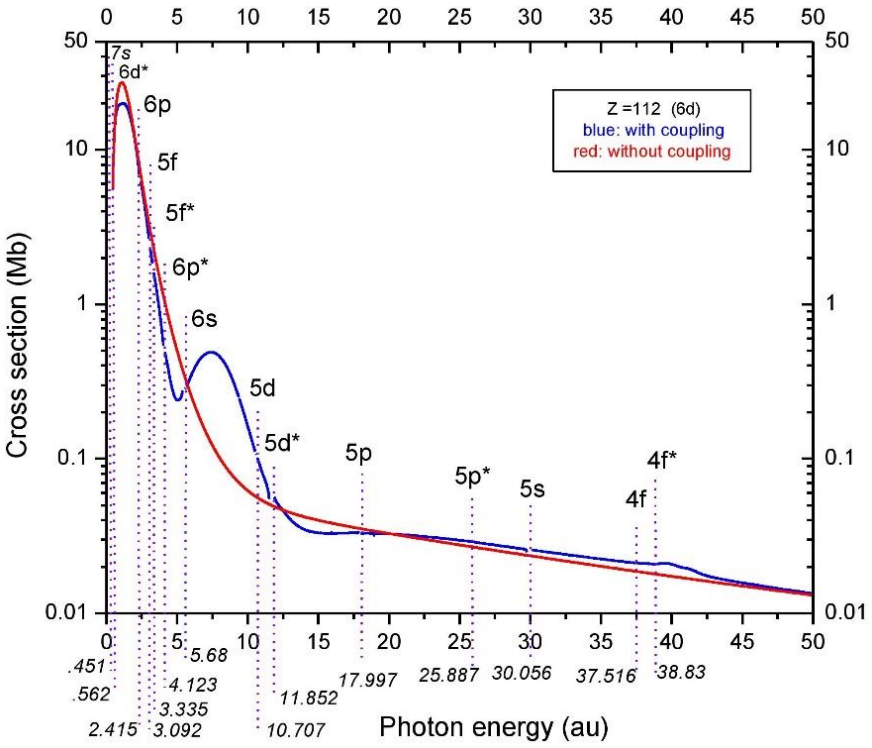

Figure 4.8: Cn 6d cross section with (blue) and without (red) coupling. Vertical lines indicate thresholds.

At still higher energies, in the 40 au region, the influence of the coupling with $4f$ and $4f^*$ becomes important, and two maxima are seen, unlike the No case; this is due to the increase in the splitting of the $4f$ and $4f^*$ thresholds at the higher Z. Note again that this is a log plot, so these alterations of the cross section are quite significant, as large as almost an order of magnitude.

As mentioned earlier, we have omitted the regions just below each threshold that are fraught with autoionizing resonances. To understand what is going on here we have performed calculations with a vastly more dense energy mesh. Specifically, instead of our usual 0.01 au mesh, we have looked at a small energy region area (0.443 au to 0.6 au) with an energy mesh of 3×10^{-4} au and the results of the calculations with the different meshes are shown in Figure 4.9. The comparison shows that the coarse mech gives completely unreliable results in this region, and even the very fine mesh gives only indications of the resonances.

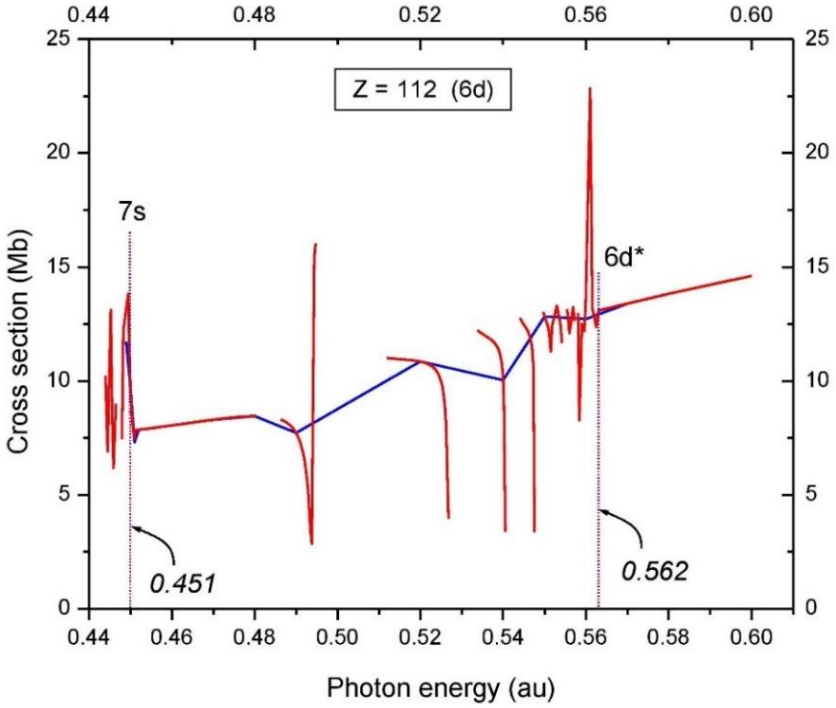

Figure 4.9: No, 6d cross section in a resonances region calculated with energy meshes of 0.01 au (blue) and 3×10^{-4} au (red). The vertical lines indicate thresholds.

The photoelectron angular distribution β parameter was also calculated with and without interchannel coupling, and the results are shown in Figure 4.10.

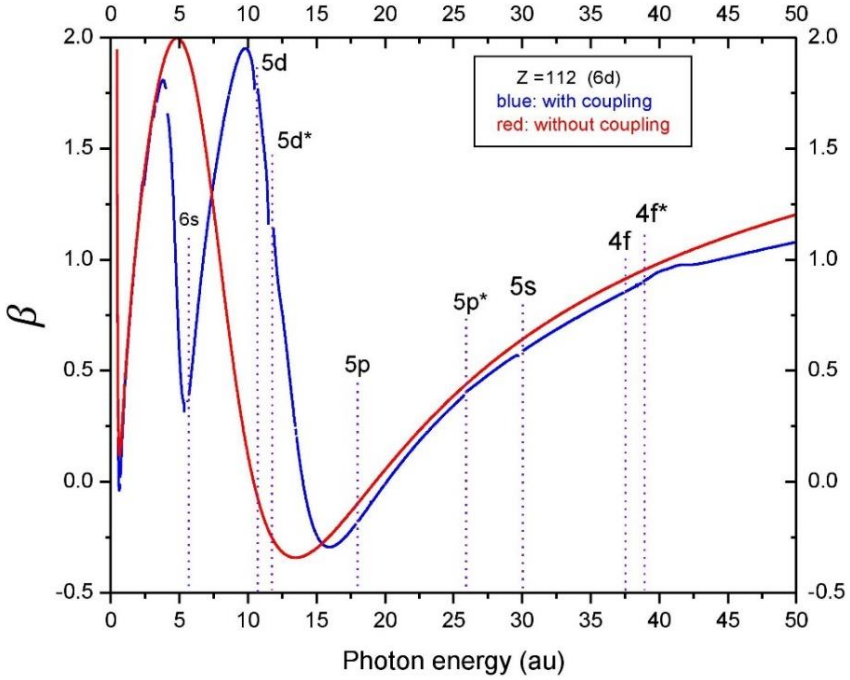

Figure 4.10: Photoelectron angular distribution parameter, β, for Cn 6d photoionization with (blue) and without (red) interchannel coupling. The vertical lines indicate thresholds.

As with the cross section, near threshold the interchannel coupling does not seem to be very important. But, in the Cooper minima regions, the β's are completely different. The existence of the altered and extra Cooper minima, induced by the interchannel coupling, are seen to have a profound effect on the β parameter. The fact that the Cooper minima have such an important impact on both the cross section and the β parameter, suggests a more detailed inquiry into them in at least this case to explore their general properties.

As discussed earlier, the cross section for a given subshell is the sum of the cross sections to the various possible final states: for the Cn, $6d$ subshell, this means $6d \longrightarrow \varepsilon p$, $6d \longrightarrow \varepsilon f^*$ and $6d \longrightarrow \varepsilon f$ photoionization channels. Furthermore, Cooper minima only exist in the $l \longrightarrow l+1$ channels. To give some idea how this works, in Figure 4.11, the results of the individual channel

cross sections along with the total $6d$ cross section is shown for the case of no interchannel coupling. The $6d \longrightarrow f, f^*$ dominate the cross section at low energy, but they both exhibit deep Cooper minima in the 10 au range; in this region the $6d \longrightarrow p$ cross section dominates the total.

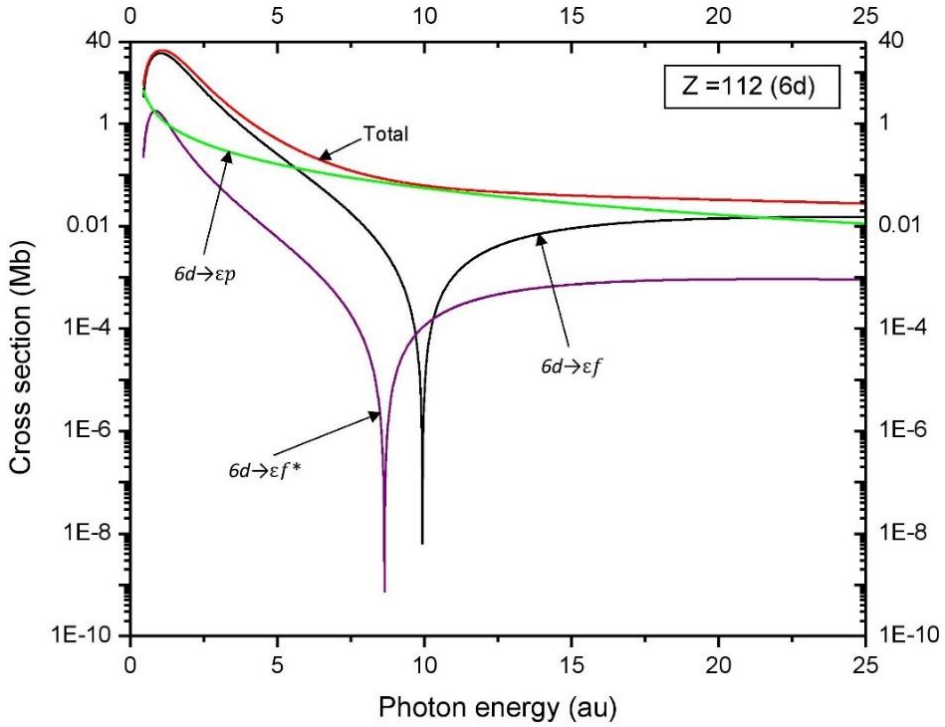

Figure 4.11: Cn, 6d cross sections for photoionization to each of the three possible final states (without coupling).

As a result, the total 6d cross section does not show evidence of a minimum, but merely a change in slope owing to the $6d \longrightarrow f, f^*$ Cooper minima.

Looking further at the Cn $6d$'s cross section, the important interchannel couplings in each energy range is examined and shown in Figure 4.12, in the same manner as was done for No 7s. From threshold to 1.5 au, the important coupling is with the $6d^*$ photoionization channels, and from 5.5 au to 20 au the dominant couplings are with the photoionization channels associated with the $5f$ and $5f^*$ subshells. In between these two regions, the combination of $6d^*$, $5f$ and $5f^*$ photoionization channels are required for quantitative accuracy.

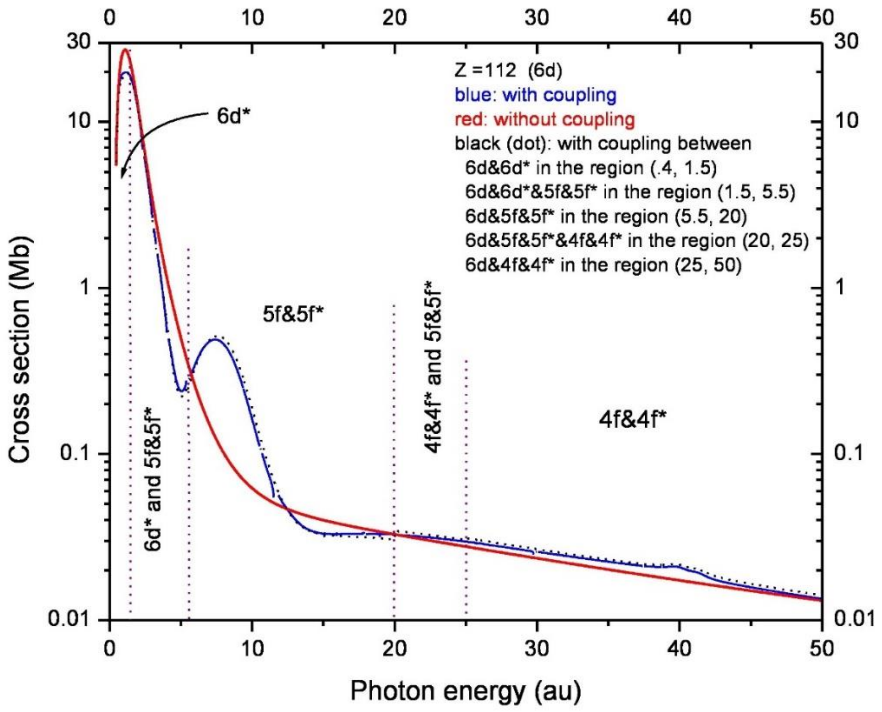

Figure 4.12: Cn, 6*d* cross section at various levels of coupling, as indicated.

Similarly, from 20 au to 25 au a combination of all of the $5f$ and $5f^*$ and $4f$ and $4f^*$ are necessary, and from 25 au to 50 au coupling with $4f$ and $4f^*$ channels are required.

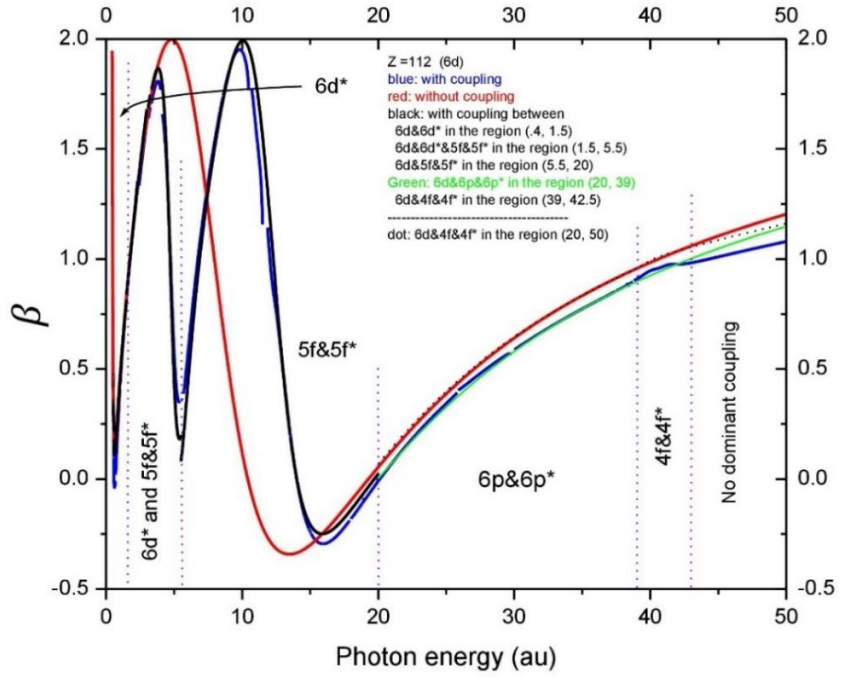

Figure 4.13: Cn, 6*d*, β parameter at various levels of coupling, as indicated.

Looking at the similar details of the Cn, 6d's β parameter, shown in Figure 4.13, a similar story is revealed, but with some small differences from the analysis of the cross section. In any case, it is clear that generally the important channels contributing to the interchannel coupling are revealed by doing the RRPA calculation at various levels of coupling.

The calculated total cross section for Cn (Z=112), both with and without coupling, is shown from threshold to 50 au (1360.6 eV) in Fig. 4.14, along with the partial cross sections of the 15 contributing subshells; all of the subshells that were included for No plus the $6d$ and $6d^*$ subshells as well. This leads to 40 coupled relativistic channels in the RRPA calculations. While these cross sections are, in a general sense, similar to the No results, there are some important differences. Over most of the energy range, the total cross section is dominated by the $5f/5f^*$ and $4f/4f^*$ subshell cross section, at low energies, below about 4 au, the $6d/6d^*$ cross sections are seen to dominate. In addition, in the region of the $5f$ shape resonances, from 5 au to 12 au, not only do the $5f$'s dominate, but every other open channel cross section in that energy range also mirrors the $5f$ shape resonances, only at much smaller magnitudes. This phenomenology can be simply explained by Eq. (4.1). The second (first order perturbation) term in Eq. (4.1) completely dominates so that each of the smaller subshell cross sections is a (smaller) copy of the $5f$ cross sections. Note also that, owing to the dominance of the $6d$ cross section near threshold, the 7s subshell acquires a Cooper minimum just where the $6d$'s have their Cooper minima, and this phenomenology, too, is a result of the interchannel coupling, as seen above.

At the higher energies, the total cross section is dominated by the $4f$ and $4f^*$subshell cross sections, and the associated $4f/4f^* \longrightarrow \varepsilon g$ shape resonances, as seen in Fig. 4.14. However, even though the $4f$ and $4f^*$ subshell cross sections are an order of magnitude or more

larger than any of the other subshell cross section in this energy region, the interchannel coupling effect is far smaller than what was seen in the $5f$ shape resonance region.

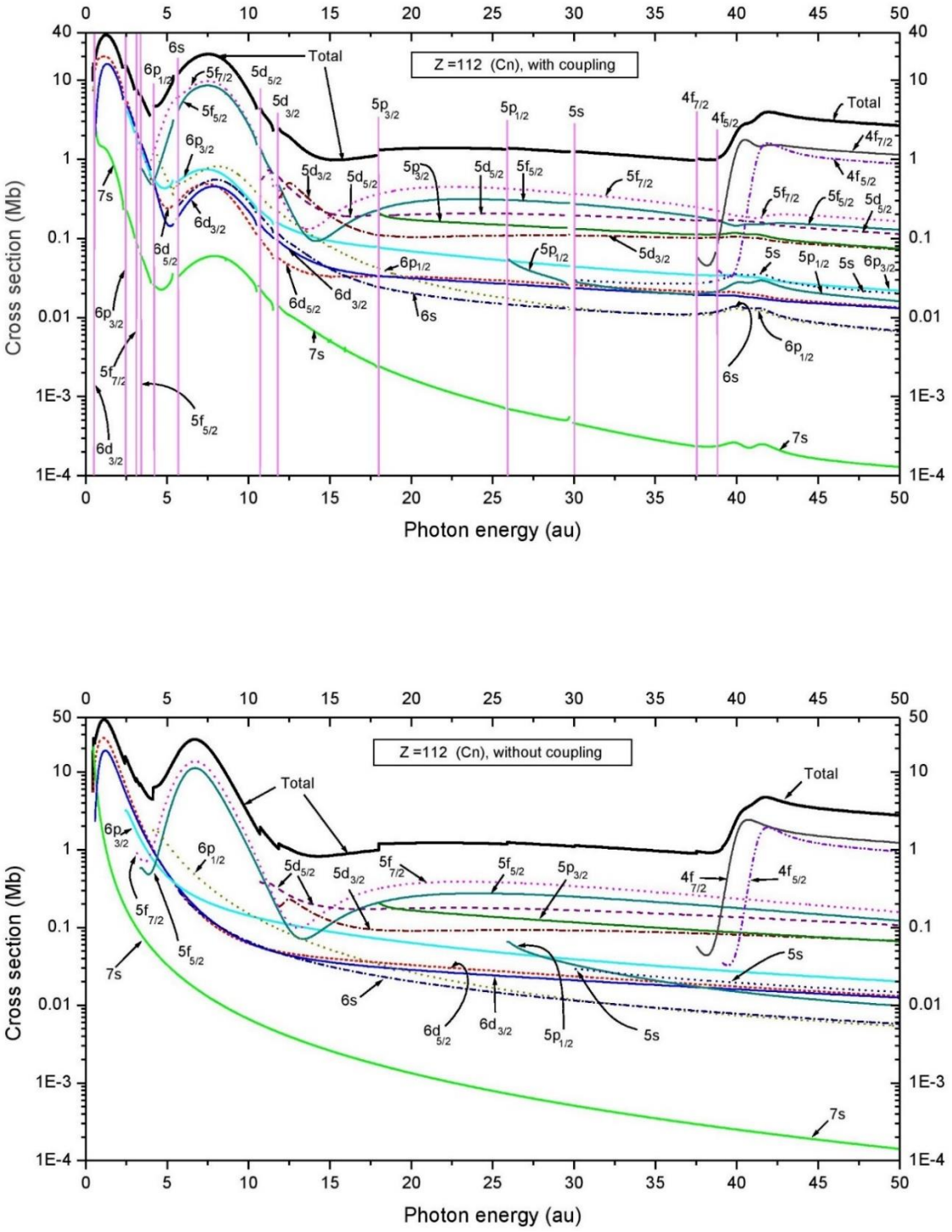

Figure 4.14: Total and subshell photoionization cross section from $6d$ to $4f^*$for Cn "with coupling" (upper panel) and "without coupling" (lower panel). The vertical lines in the upper curve indicate the various subshell thresholds.

Why should this be? The answer lies in the nature of the interchannel coupling matrix element, $\langle \psi_i(E) | H - H_0 | \psi_j(E') \rangle$. There is both a direct and exchange part of this matrix element. In the direct term, the $5f$ orbital overlaps reasonably well with the nearby subshell orbitals since they are roughly the same size; whereas the $4f$ and $4f^*$ orbitals are considerably smaller (more compact) than the orbitals associated with any of the open channels in the higher energy range, thereby rendering the direct interchannel coupling matrix element much smaller in the $4f$ case. Furthermore, for the exchange term, in the $5f$ and $5f^*$ cases, the continuum wave functions of the weaker channels have relatively low photoelectron energy, just a few au, so they are not very oscillatory; in the $4f$ and $4f^*$cases, the continuum wave functions for the weaker channels exhibit much higher photoelectron energy, in the region of the $4f$ and $4f^*$shape resonances, so that they are very oscillatory and this makes the $4f$ exchange matrix elements considerably smaller than the $5f$ case. For these reasons, the interchannel coupling effects should be much smaller in the neighborhood of the 4f shape resonances, just as seen in Fig. 4.14. It turns out that the best overlap for the $4f$ and $4f^*$ orbitals is with the $5p^*$ subshell, and it is also one of the closest subshells energetically. Thus, it would be expected that the interchannel coupling effect, although small, would be largest for the $5p^*$ cross section, an expectation that is borne out in Fig. 4.14. From this discussion, it is evident that the detailed manifestation of interchannel coupling, in each case, is a complicated business.

It is also seen that the $4f$ cross section exhibits a kink just above its maximum, in the vicinity of the $4f^*$ maximum. This is an effect that was discovered in lighter atoms, particularly in nd subshells, and is known as spin-orbit-interaction-activated interchannel coupling (SOAIC) [**20, 68**]. Basically, owing to the spin-orbit interaction, the nonrelativistic $4f$ subshell is split into a doublet, $4f$ and $4f^*$, and there is an interchannel interaction between the photoionizing

channels of each member of the doublet, between the $4f$ and $4f^*$ channels, in this case. It is this interchannel interaction that creates the structure in the 4f cross section, that can only occur owing to the spin-orbit splitting of the $4f$'s; hence the name.

The ratio of "with" versus "without" coupling is shown in Figure (4.15). Like No, the figure omits the nl^* to uncomplicate the figure. From this depiction it is evident that over a broad region of energy centered around 10 au, the cross section is dominated by interchannel coupling with the $5f$and $5f^*$ photoionization channels.

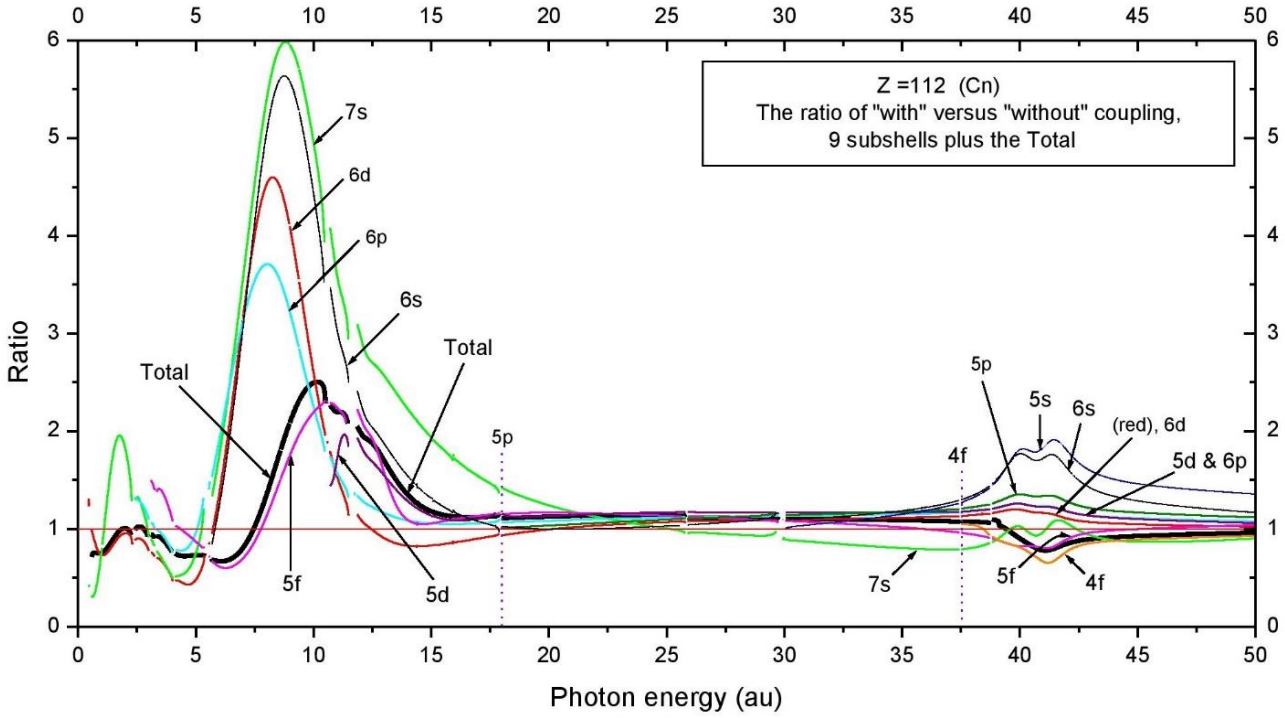

Figure 4.15: Ratio of subshell and total Cn photoionization cross sections "with" and "without" interchannel coupling. The vertical lines indicate thresholds.

And in the 40 au region, the same is true for the $4f$ and $4f^*$ although, for reasons discussed in connection with No, the effects not so great here. In addition, near threshold, the 7s cross section is seen to be affected strongly by coupling with the $6d$ and $6d^*$ channels.

B- Confined in quantum well

As mentioned in Section **2.8**, confining the atom in a cage (the molecule C_{60}) results alterations of the results. The consequence of confinement for energies is indicated in a shortened Table 4.1 where small changes in binding energies of Cn are seen in comparison to the free atom energies. But ordering is not changed, even for the delicate balance of the three outermost subshells. For the inner shells, since they are well inside the confining well, the energies are all increased by just about the same amount, with a slightly smaller change for the outermost subshells. The Cn atom confined in the C_{60} molecule is referred to as Cn@C_{60}.

Table 4.1: Subshell binding energies for free and confined Cn, Cn@C_{60}.

Dirac-Fock Levels for Cn, Z = 112			
	shell	free atom	confined atom
1	$1s$	-7070.7147734	-7070.7301242
2	$2s$	-1444.8456191	-1444.8607427
3	$2p^*$	-1405.7154919	-1405.7306996
4	$2p$	-1007.0985135	-1007.1136691
*	****	**********	**********
23	$6p^*$	-4.1231458	-4.1382444
24	$5f^*$	-3.3349698	-3.3500539
25	$5f$	-3.0925268	-3.1075715
26	$6p$	-2.4156562	-2.4300784
27	$6d^*$	-0.5627333	-0.5764536
28	$7s$	-0.4511341	-0.4600834
29	$6d$	-0.4420894	-0.4548515

In the table, nl indicates $j = l + \frac{1}{2}$; nl^* *indicates* $j = l - \frac{1}{2}$

A general feature of the photoionization cross sections of confined atoms are oscillation known as confinement that were predicted in the early 1990's [**69**]. These oscillations, or resonances arise from the interference of a photoelectron wave emitted directly and one reflected from the confining well [**70**]. At one time, these resonances were thought to be just a theoretical artifact [**71**], but experiment has confirmed their existence [**72**]. These oscillations depend primarily upon the geometry of the confinement.

Figure 4.16 displays the oscillations of the 5d cross section of Cn@C_{60} for both "with" and "without" coupling. It shows clearly that the confinement oscillations are essentially the same, wherether or not coupling is included, thereby confirming that the oscillations are essentially geometric in character. Of interest here are the facts that the confined cross sections are essentially oscillations about the free cross section, and the confinement oscillations diminish in amplitude with increasing photoelectron energy.

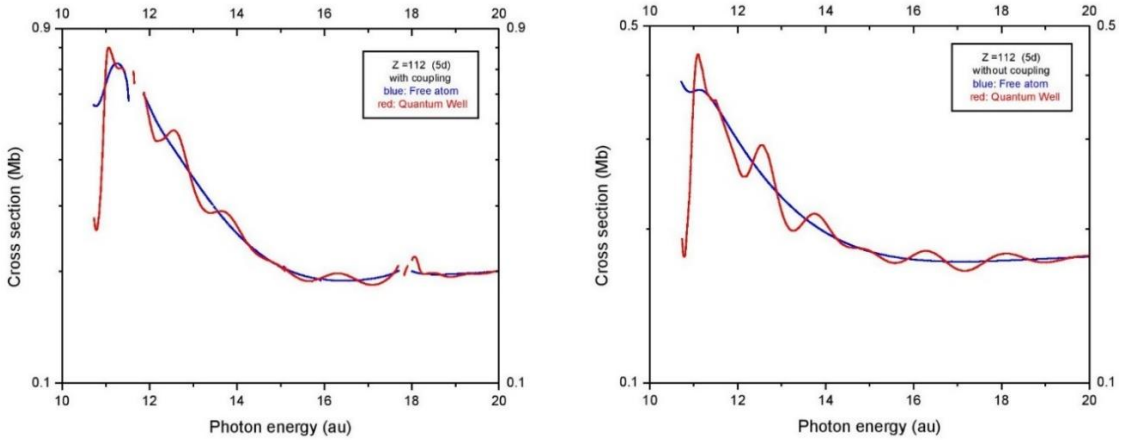

Figure 4.16: Photoionization cross section of the 5d subshell of Cn@C_{60} and free Cn including coupling (left panel) and without coupling (right panel).

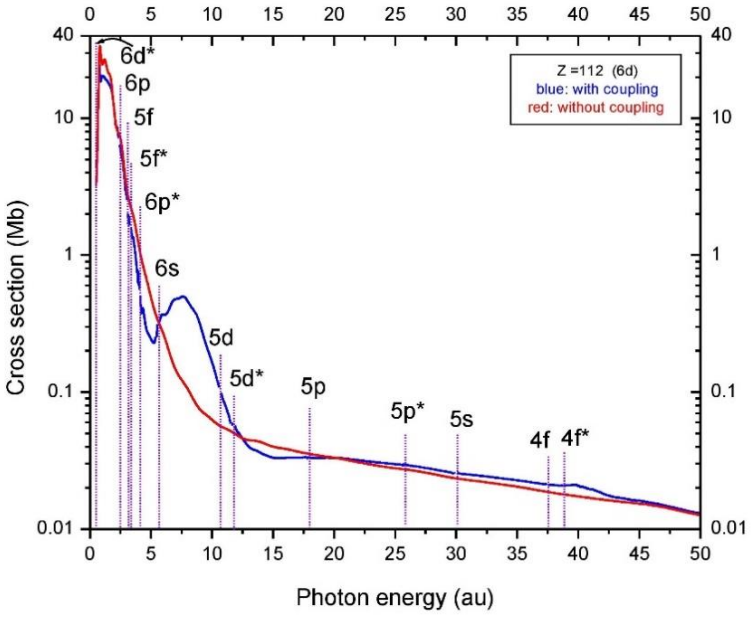

Figure 4.17: Photoionization of the 6d subshell of Cn@C_{60} with coupling (blue) and without coupling (red). The vertical lines show the thresholds.

To further illustrate the point, the confined $6d$ cross section is shown in Figure 4.17 with and with coupling. Since this is given on a log scale the differences between the confined and free results (Figure 4.8) are barely perceptible. Note further that the oscillations are in the dipole matrix elements so that they will be there for all photoionization parameters, e.g., the β parameter.

Similar to free atom, the calculation has been repeated for the cross sections of all 15 subshells for the atom inside the confining potential well representing the effects of the C_{60}, and the results are presented in Figure 4.18 along with the total cross section. Comparison with the results for the free Cn atom, Figure 4.14, the only differences are, aside from the small shifts in thresholds, the confinement resonances which shows up very small wiggles on this log plot.

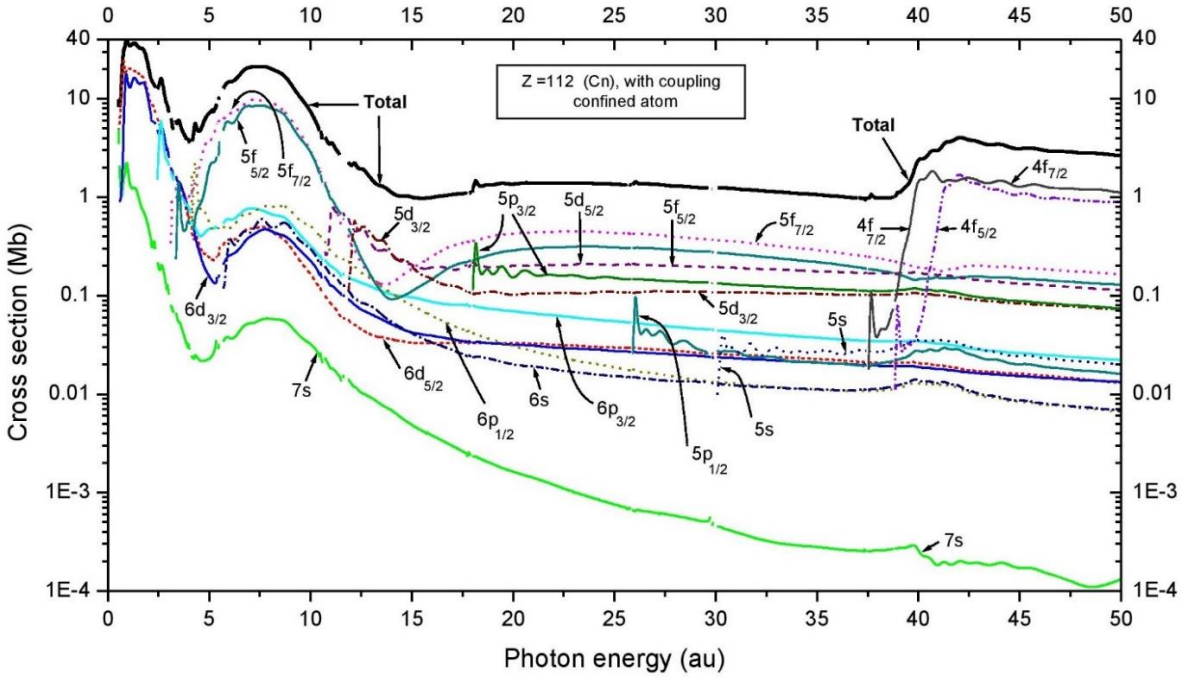

Figure 4.18: Total and subshell crosss section for Cn@C_{60} including coupling.

4.3 Oganesson (Z=118)

Og is the heaviest element that has been synthesized in the laboratory. We start with the outermost, $7p$, subshell and the photoionization cross section is shown in Figure 4.19 with and

without interchannel coupling. The overall shape of the two plots in Figure 4.19 are similar to Cn with significant structure due to coupling with $6d/6d^*$ channels in the 2 au to 3 au range, and with the $5f/5f^*$ channels in the 8 au to 15 au range. The coupled results show two obvious munima regions; one of them between 1.6 and 2 au consists of two Cooper minima very near together. Also there is a Cooper minimum in the uncoupled result, but they do not show up as a minumum in the cross section, similar to previous cases. It is odd though that is no evident structure in the region of the $4f/4f^*$ channels.

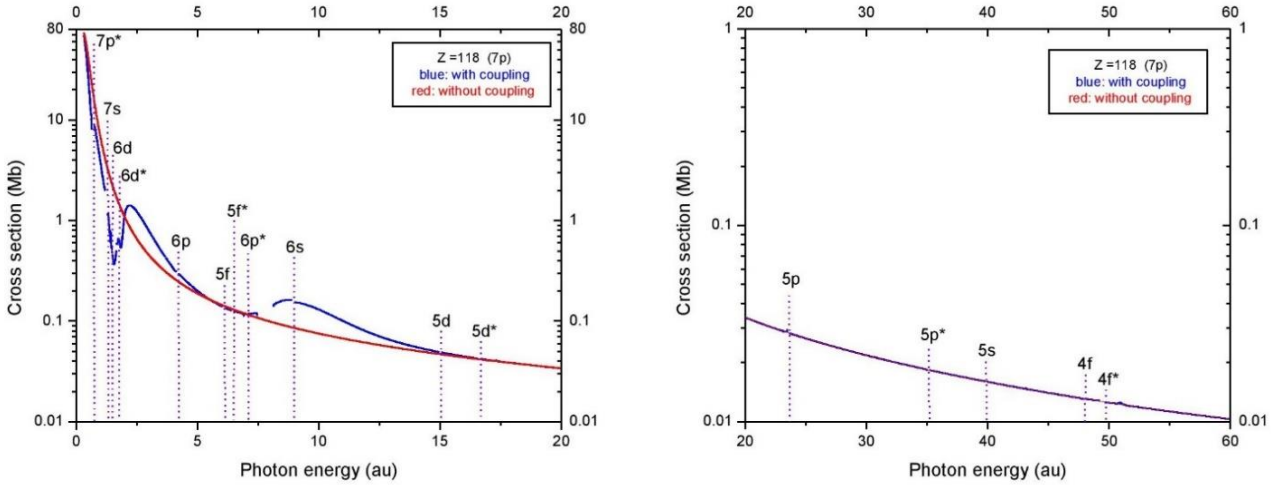

Figure (4.19): Og, 7p cross section with (blue) and without (red) coupling. Vertical lines indicate thresholds.

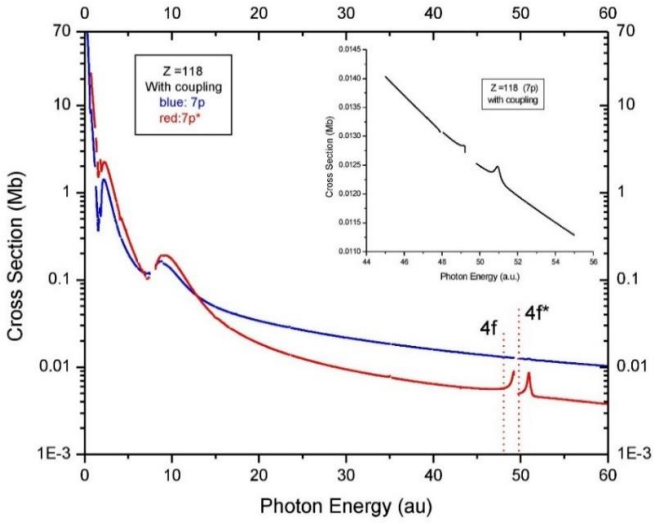

Figure (4.20): Og, 7p (blue) and 7p* (red) cross sections with full coupling. A magnified view of the 7p cross section is shown in the inset.

To investigate this matter further, in Figure 4.20 the $7p$ and $7p^*$ cross sections with full coupling are shown. As seen in this plot, the $7p^*$ cross section clearly displays the interchannel coupling effects of the $4f$ and $4f^*$ channels, but $7p$ shows almost nothing. Looking at the inset in Figure 4.20 the existence of the effect of coupling is evident but extremely small. To understand this behavior we have performed truncated RRPA calculations, calculations omitting certain channels as indicated, and the results are given in Figure 4.21. From this figure it is evident that in the $7p$ case, the effects of interchannel coupling with the $4f$ and $4f^*$ channels are in opposite directionss, so the interchannel effects are almost cancelled out, but this is not the case for the $7p^*$ cross section so that the signature of coupling in this region is strong.

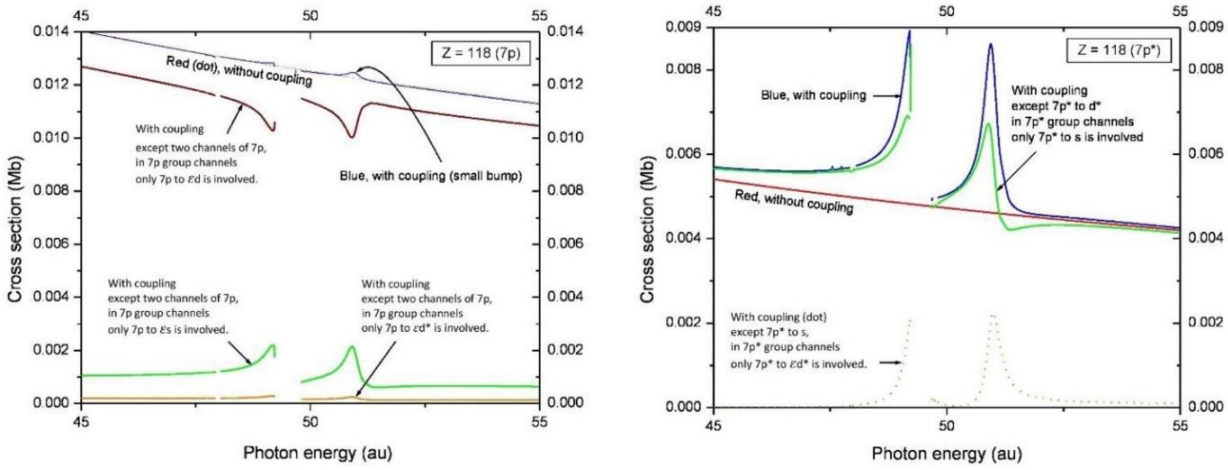

Figure (4.21): Og, $7p$ (left panel) and $7p^*$ (right panel) cross sections in the region of the $4f$ and $4f^*$ thresholds calculated at various levels of truncation.

Looking at the angular distribution β parameter for Og, 7p photoionization, shown in Figure 4.22, for both with and without interchannel coupling shows the huge importance of the coupling over a broad range of energies; over certain energy ranges the coupled β parameter is vastly different from the uncoupled result. Furthermore, the effect of coupling with the $4f$ and $4f^*$ subshell cross sections is very evident, unlike the cross section as described above. This

shows that the cross section and the β parameter reveal different aspects of the physics of the photoionization process.

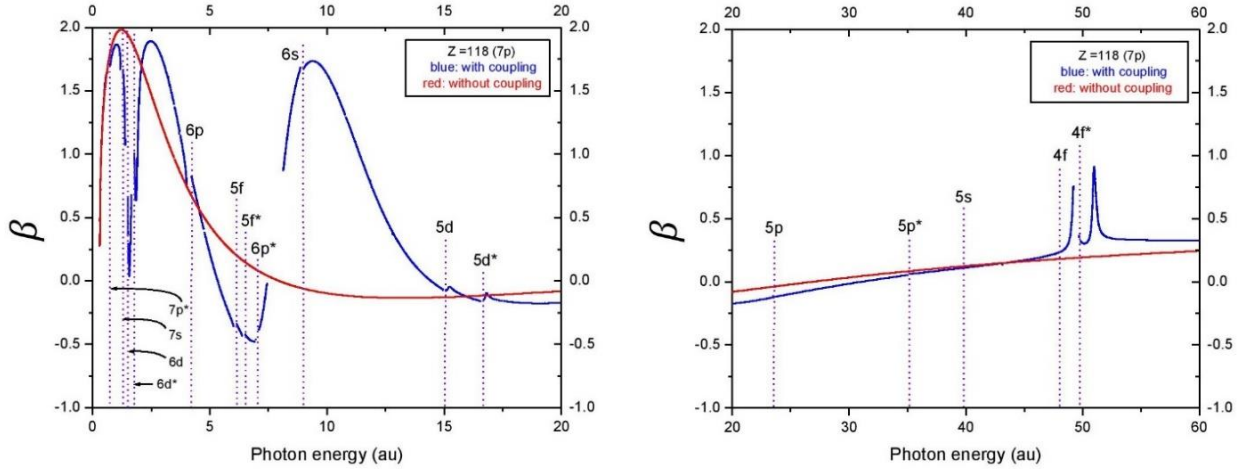

Figure (4.22): Og, 7p, β parameter with and without coupling.

As was done in the previous cases, truncated RRPA cross section calculations were performed at various levels to determine the dominant subshells involved in the interchannel coupling in each energy region and the results are shown in Figure 4.23. The vertical scale for the right plot is different to make it easier to see the cross section at the higher energies. From these results it is clear that in most the dominant couplings are easily identified.

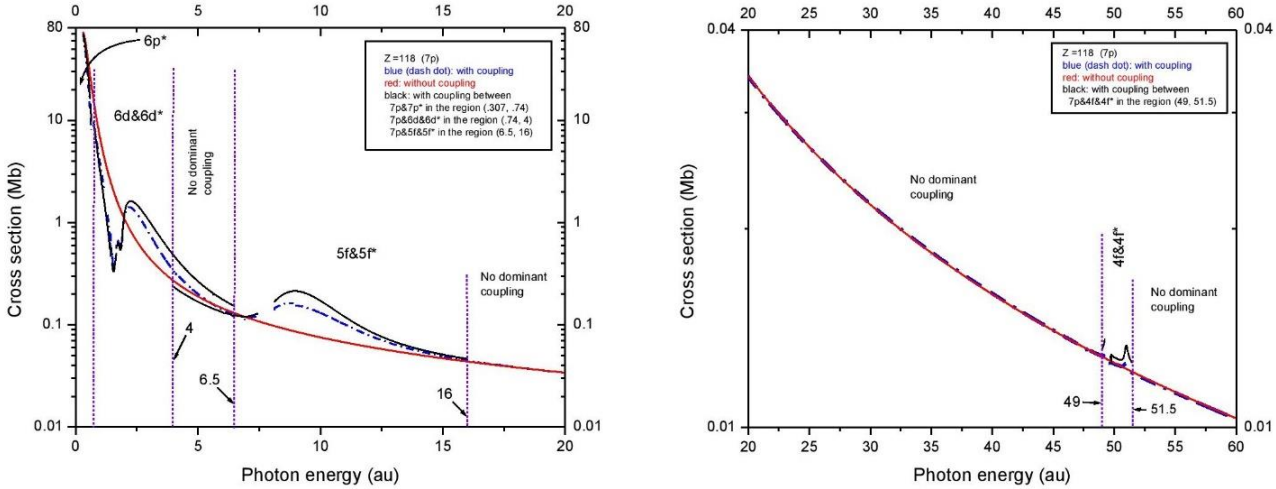

Figure (4.23): Og, 7*p* cross section at various levels of coupling, as indicated.

Similarly, this exercise was repeated for the $7p$, β parameter and the β's, calculated at different levels of coupling, are given in Figure 4.24. The results, as related to the important contributions of the interchannel coupling in the various energy ranges, are seen to be pretty much the same as for the cross section.

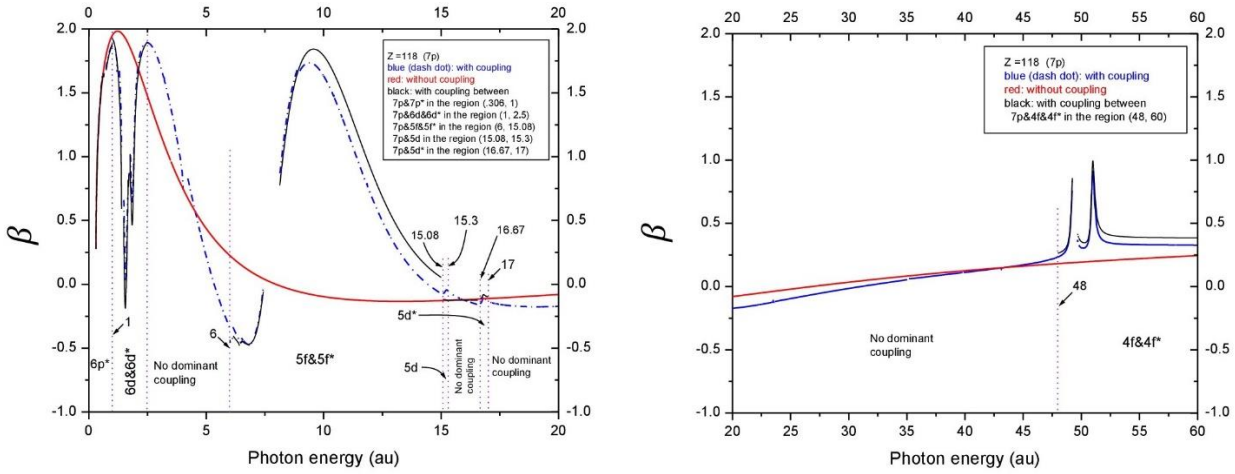

Figure (4.24): Og, $7p$, β parameter at various levels of coupling, as indicated.

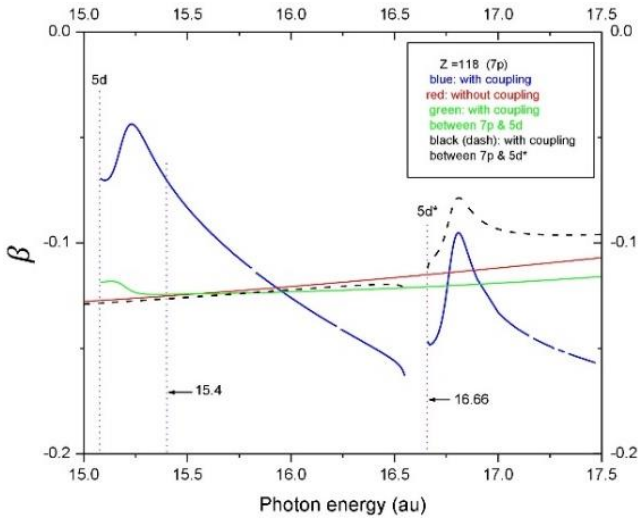

Figure (4.25): Og, $7p$, β parameter at various levels of coupling, as indicated; magnification of the energy region from 15 to 17.5 au.

However, the $4f$ and $4f^*$ channels are much more important in β. In addition. There is a small effect of the $5d$ and $5d^*$channels, shown in Figure 4.25, that is essentially absent for the cross section.

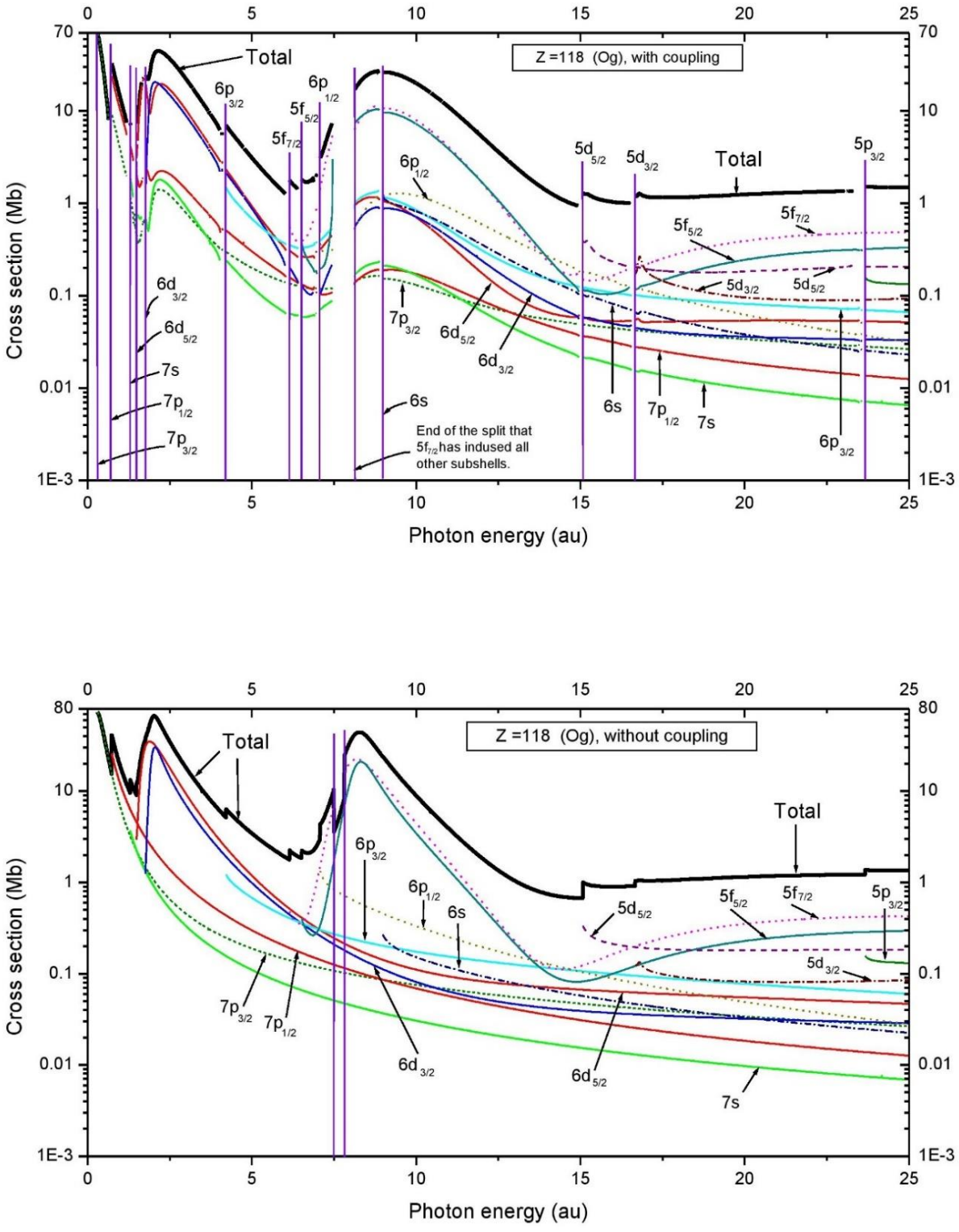

Figure 4.26: Total and subshell photoionization cross section from $6d$ to $4f^*$ for Og "with coupling" (upper panel) and "without coupling" (lower panel) in the energy range from threshold to 25 au. The vertical lines in the upper curve indicate the various subshell thresholds.

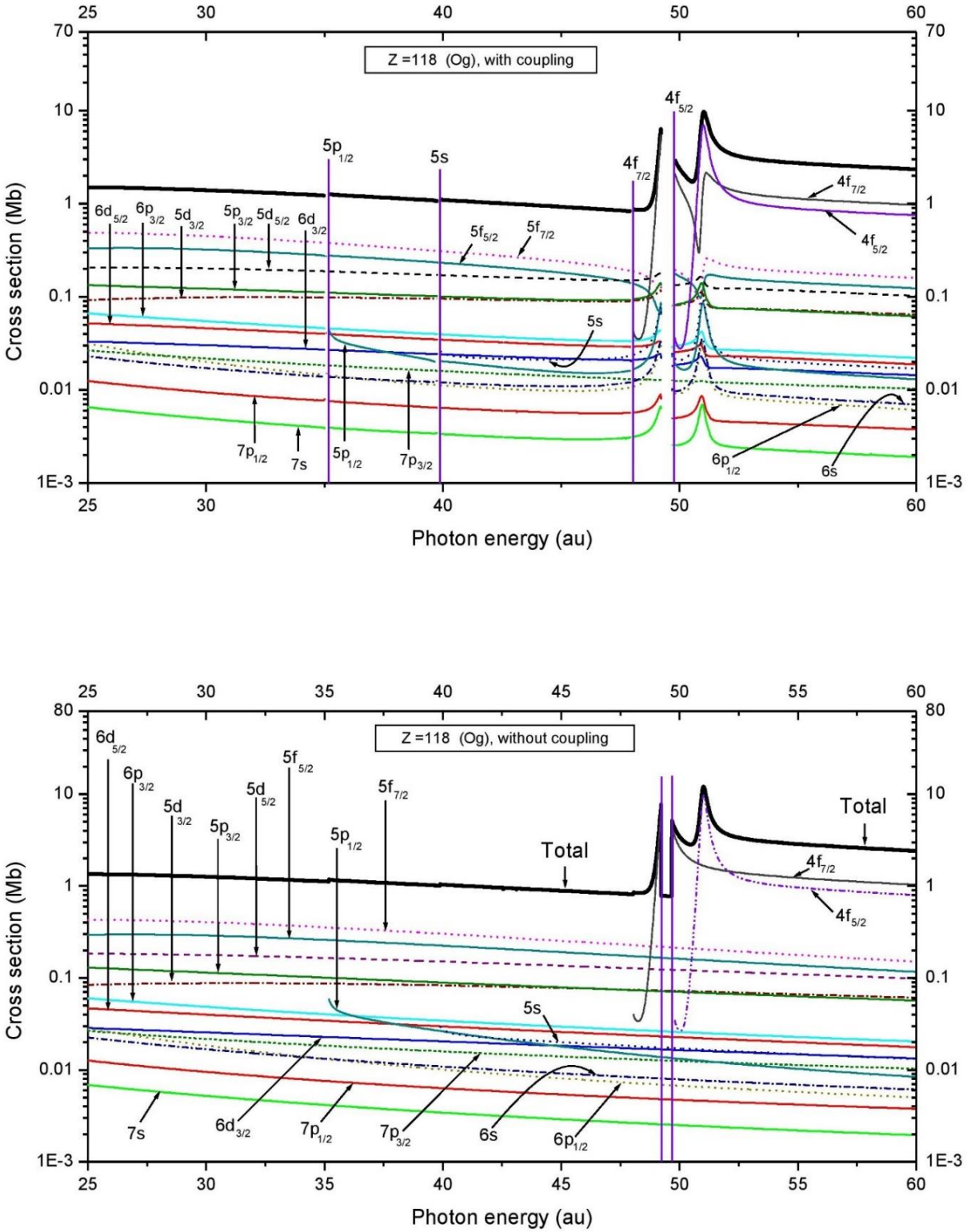

Figure (4.27): Total and subshell photoionization cross section from $6d$ to $4f^*$ for Og "with coupling" (upper panel) and "without coupling" (lower panel) in the energy range from 25 au to 60 au. The vertical lines in the upper curve indicate the various subshell thresholds.

The total photoionization cross section for Og, Z=118, is shown in Figures 4.26 and 4.27 from threshold to 60 a.u. (1,632.7 eV), along with the subshell cross sections for all of the 17 contributing subshells, i.e., all of the subshells included for Cn, plus $7p$ and $7p^*$, which leads to 45 interacting channels in the RRPA calculation.

The results are, in a general sense, quite similar to the Cn cross sections. Over most of the energy range the $6d/6d^*$, $5f/5f^*$ and $4f/4f^*$ subshells are seen to dominate the total cross section, except in the region of the $5f/5f^*$ Cooper minima where the $5d/5d^*$ cross sections are dominant over a small energy range. And interchannel coupling is even more important for Og than it was for Cn. In the region where the $6d$'s dominate, all of the cross sections of the weaker subshells mimic the $6d$'s, and similar results are seen for the region of the $5f$ shape resonances. This means, of course, that it is the second term in Eq. (4.1), the perturbation term, which dominates the subshell cross sections. In other words, the first term, the single-particle contribution to the dipole matrix elements is small so that the dipole matrix elements for these weaker subshells are dominated by many-body interactions, i.e., correlation.

Like the first two elements, The ratio of "with" versus "without" coupling is shown for only nl cross sections of Og subshells (Figure 4.28).

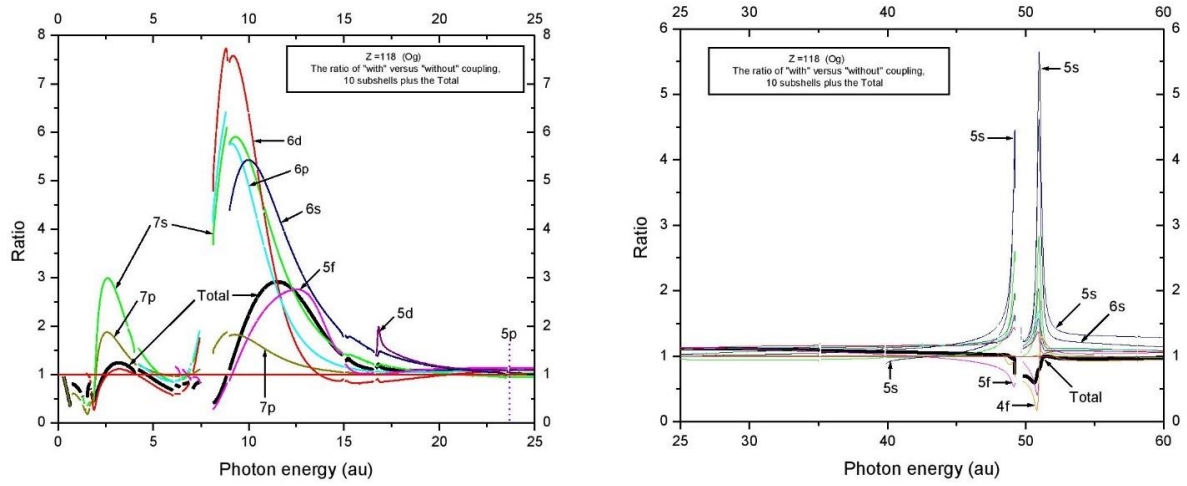

Figure 4.28: Ratio of subshell and total Og photoionization cross sections "with" and "without" coupling.

In this case the greatest change belongs $6d$ then $6p$, 7s and 6s. In the interval between about 20 and 45 au almost all ratios are parallel and near unity showing that interchannel coupling is not important here. Similar to the previous cases, above the $4f$ and $4f^*$, interchannel coupling is again seen to be important and the coupling affects different subshells differently in the sense that some of the cross sections increase and others decrease under influence of coupling.

It is noteworthy that even in the $4f/4f^*$-dominated region, the cross sections of the weaker subshells clearly take on the form of the $4f/4f^*$ cross sections; for Cn there was only a hint of the interchannel coupling in the $4f$-dominated region. The reason for this difference is that the $4f/4f^*$ peaks in the Og cross section are about two orders of magnitude larger than the next largest subshell cross sections, while in Cn the difference is only about one order of magnitude, so that the interchannel coupling contribution to the smaller subshell cross sections, the second term on the right-hand side of Eq. (4.1), is proportionately, a factor of ten larger.

5 CONCLUSIONS

Photoionization cross sections of the ground states of the closed subshell superheavy elements No (Z=102), Cn (Z=112) and Og (Z=118) have been performed using the sophisticated fully relativistic RRPA methodology. The total photoionization cross sections, in all three elements, were dominated by the $5f/5f^*$ and $4f/4f^*$ subshells over a broad range of photon energies, and for Cn and Og, by the $6d/6d^*$ subshells near the thresholds. In addition, the smaller subshell cross sections were found to be, in almost all cases, reduced versions of the dominant subshell cross sections in each energy range, a testament to the importance of interchannel coupling. In addition, in many cases for inner subshells, the spin-orbit splitting is so

large that the dynamics of the two members of many inner-shell spin-orbit doublets are completely different from one another, e.g., the $5p$ and $5p^*$ cross sections in all three cases studied.

In addition, for the inner shells, No is quite normal in the threshold energy ordering compared to it lower-Z homologues, but for both Cn and Og, both the $5f$ and $5f^*$ levels lie between the $6p$ and the $6p^*$ levels owing to the huge $6p/6p^*$ spin-orbit splitting in those two cases. This finding demonstrates the strength of relativistic interactions in these high-Z atoms.

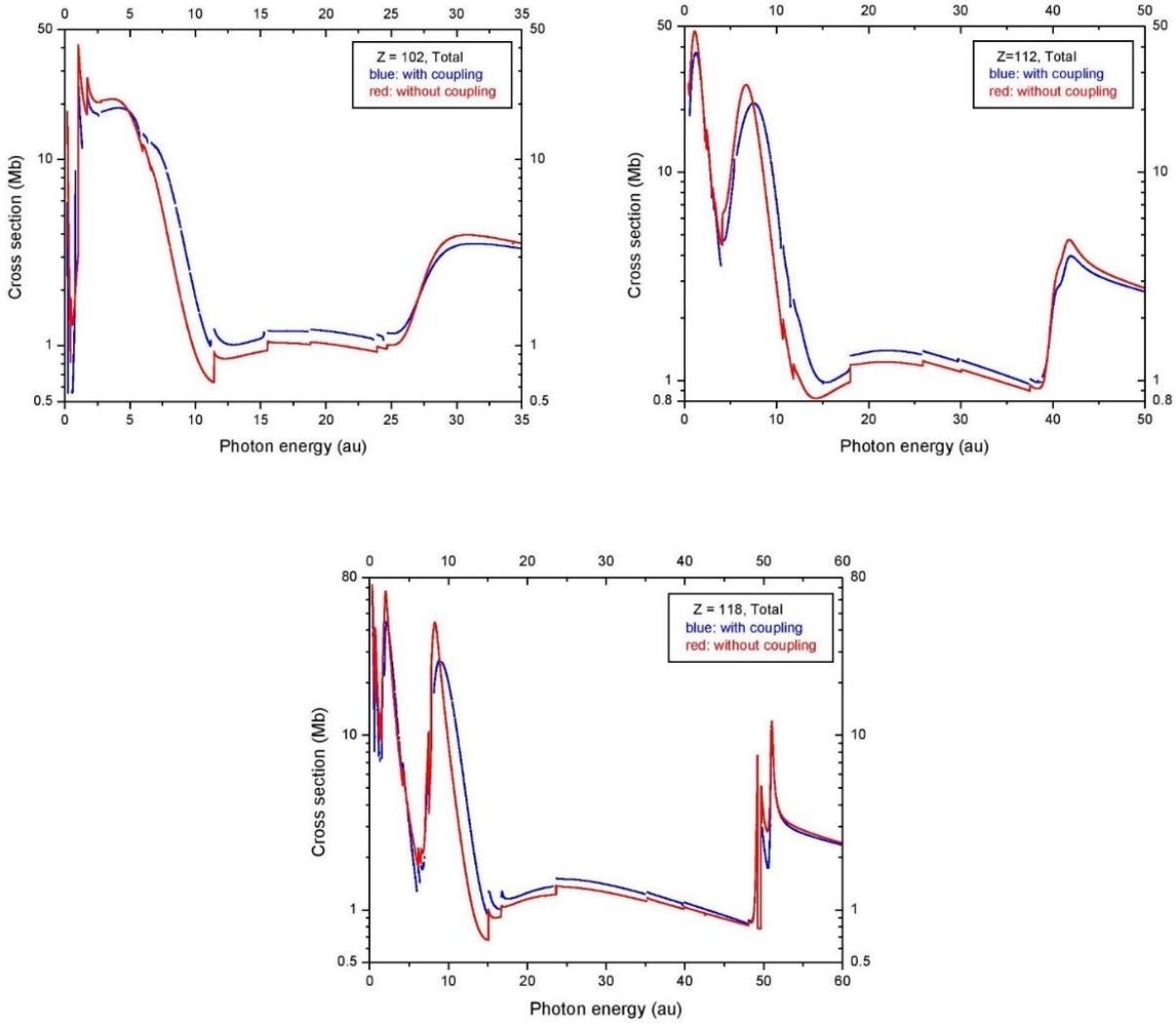

Figure 5.1: Similarity between "without" plot of total of cross sections and "with coupling" plot for the three elements.

Although interchannel coupling was found to be crucial important for most subshells of all three elements over most of the energy range condsidered, this amounted to a redistribution of oscillator strength, so the total cross sections were not so severely affected. To emphasize this point, the total cross sections for No, Cn and Og are shown in Figure 5.1 both with and without coupling and it is evident that the overall qualitative and quantitative agreement between them is reasonably good.

Now, except that the atomic systems studied are closed subshell systems, there is nothing special about No, Cn and Og compared to the other nearby atoms in the periodic table. Thus, it is evident, that similar interchannel coupling effects in the photoionization can be expected for all of the superheavy elements, along with perhaps other surprises owing to the combined multiplet and spin-orbit effects in the valence shells of open-shell atoms. In other words, the phenomenology described herein should be quite general.

REFERENCES

1. N. Bohr, *On the Constitution of Atoms and Molecules*, Phil. Mag. **26**, 1-24 (1913).
2. J. P. C. Mbagwu, Z. L. Abubakar, J. O. Ozuomba, *A Review Article on Einstein Special Theory of Relativity*, Int. J. of Theor. Math. Phys., **10**, 65-71 (2020).
3. P. Pyykkö, and J. P. Desclaux, *Relativity and the periodic system of elements*, Acc. Chem. Res. **12**, 276–281 (1979).
4. C. Qiao, H. Chi, M. Hsu, X. Zheng, S. Jiang, S. Lin, C. Tang, K. Huang, *Photoionization of Xe and Rn from the relativistic random-phase theory*, J. Phys. B: At. Mol. Opt. Phys. **52**, 075001 (2019).
5. A. K. Razavi, R. K. Hosseini, D. A. Keating, P. C. Deshmukh and S. T. Manson, *Photoionization of superheavy atoms: correlation and relativistic* effects, J. Phys. B: At. Mol. Opt. Phys. **53**, 205203 (2020).
6. H. Kragh, *The search for superheavy elements: Historical and philosophical perspectives*, arXiv:1708.04064v1 (2017).
7. P. A. M. Dirac, *Quantum mechanics of many-electron systems*, Proc. R. Soc. Lond. A **123**: 714 –733 (1929).
8. Y. Ts. Oganessian and S. N. Dmitriev, *Synthesis and study of properties of superheavy atoms. Factory of Superheavy Elements*, Russ. Chem. Rev. **85**, 901-916 (2016).
9. M. E. Wieser, *Atomic weights of the elements 2005,* Pure Appl. Chem. **78**, 2051-2066 (2006).
10. S. K. Cary, M. Vasiliu, R. E. Baumbach, J. T. Stritzinger, T. D. Green, K. Diefenbach, J. N. Cross, K. L. Knappenberger, G. Liu, M. A. Silver, A. Eugene

DePrince, M. J. Polinski, S. M. V. Cleve, J. H. House, N. Kikugawa, A. Gallagher, A. A. Arico, D. A. Dixon, and T. E. Albrecht-Schmitta, *Emergence of californium as the second transitional element in the actinide series*, Nature Comm. **6**, 6827 (2015).

11. J.-M. Mewes, O. R. Smits, G. Kresse, P. Schwerdtfeger, *Copernicium is a Relativistic Noble Liquid,* Ang. Chem. **131,** 18132-18136 (2019).
12. D. Rabinovich, *Oganesson, Where Art Thou?*, Chem. Int. **40**, 4 (2018).
13. K. Chapman, *The oganesson odyssey*, Nature Chem **10**, 796 (2018).
14. H. Kragh, *Max Planck: the reluctant revolutionary*, Phys. World **13**, 31-35 (2000).
15. V. L. Jacobs, *Theory of atomic photoionization measurements*, J. Phys. B: Atom. Mol. Phys. **5**, 2257-2271 (1972).
16. D. A. Verner and D. G. Yakovlev, *Analytic FITS for partial photoionization cross sections*, Astron. Astrophys. Suppl., **109**, 125-133 (1995).
17. M. Ya. Amusia, L. V. Chernysheva, S. T. Manson, A. M. Msezane, and V. Radojević, S*trong Electron Correlation in Photoionization of Spin-Orbit Doublets*, Phys. Rev. Lett. **88**, 093002 (2002).
18. T. D. Thomas, E. Kukk, K. Ueda, T. Ouchi, K. Sakai, T. X. Carroll, C. Nicolas, O. Travnikova, and C. Miron, *Experimental Observation of Rotational Doppler Broadening in a Molecular System*, Phys. Rev. Lett. **106**, 193009 (2011).
19. O. Hemmers, G. Fisher, P. Glans, D. L. Hansen, H. Wang, S. B. Whitfield, D. W. Lindle, R. Wehlitz, J. C. Levin, I. A. Sellin, R. C. C. Perera, E. W. B. Dias, H. S. Chakraborty, P. C. Deshmukh and S. T. Manson, *Beyond the Dipole*

Approximation: Angular-Distribution Effects in Valence Photoemission, J. Phys. B: At. Mol. Opt. Phys. **30**, L727 (1997).

20. D. Toffoli, M. Stener and P. Decleva, *Application of the relativistic time-dependent density functional theory to the photoionization of xenon*, J. Phys. B: At. Mol. Opt. Phys. **35**, 1275 (2002).
21. P.C. Deshmukh and S. T. Manson, *Photoionization of magnesium in the relativistic random-phase approximation*, Phys. Rev., A **28**, 209 (1983).
22. D. A. Keating, "*Evolution of Relativistic Effects in the Photoionization of Free and Confined Heavy Atoms*." Dissertation, Georgia State University (2018).
23. H. W. Kroto, C_{60}^{B} *buckminsterfullerene, other fullerenes and the icospiral shell*, Comp. Math. Applic. **17**, 417-423 (1989).
24. W. R. Johnson and C. D. Lin, *Multichannel relativistic random-phase approximation for the photoionization of atoms*, Phys. Rev. A **20**, 964 (1979).
25. M. H. Javani, "*Photoionization of Fullerens and Atoms Confined in Fullerenes*." Dissertation, Georgia State University (2014).
26. H. Pathak, S. Sasmal, M. K. Nayak, N. Vaval, and S. Pal, *Relativistic equation-of-motion coupled-cluster method for the electron attachment problem*, Comp. Theor. Chem. **1076,** 94-100 (2015).
27. Li, J., Dong, C., Yu, Y. et al, *The atomic structure and the properties of ununbium (Z = 112) and Mercury (Z = 80)*, Sci. China Ser. G-Phys. Mech. Astron. **50**, 707–715 (2007).
28. J. J. Sakura, *Advanced Quantum Mechanics*, Reading, Mass: (Addison-Wesley, Reading, MA, 1967).

29. C. T. Sebens, *Electromagnetism as Quantum Physics*, Found. Phys. **49**, 365-389 (2019).

30. H. Bruus, K. Flensberg, *Many-Body Quantum Theory in condensed Matter Physics*, (CPI Group (UK) Ltd, Groydon, 2016).

31. S. Raimes, *Many-electron theory*, (North-Holland Publishing Company, Amsterdam, 1972).

32. R. Gerritsma, G. Kirchmair, F. Zähringer, E. Solano, R. Blatt, C. F. Roos, *Quantum simulation of the Dirac equation*, Nature **463**, 68-71 (2010).

33. H. Kragh, *The genesis of Dirac's relativistic theory of electrons*, Arch. Hist. Exact Sci.Mech. **24**, 31–67 (1981).

34. J. T. Cremer, *Neutron and X-ray Optics* (Elsevier, Amsterdam, 2013).

35. M.A. Thomson, *The Dirac Equation*, (Cambridge University Press, London, 2011).

36. D. S. Durfee and J. L. Archibald, *Applying classical geometry intuition to quantum spin*, Eur. J. Phys. **37**, 055409 (2016).

37. A. Kojevnikov, V. Vizgin, Y. Balashov, *Einstein Studies in Russia "Dirac's Quantum Electrodynamics"*, (Springer, Berlin, 2002).

38. I. P. Grant, *Relativistic Quantum Theory of Atoms and Molecules: Theory and Computation*, (Springer, Berlin, 2007).

39. A. Szabo and N. S. Ostlund, *Modern Quantum Chemistry : Introduction to Advanced Electronic Structure Theory*, (Dover Publications, New York, 1996).

40. W. Müller, C. Nager, P. Rosmus, *The frozen orbital approximation for calculating ionization energies with application to propane*, Chem. Phys **51**, 43-48 (1980).

41. S K. Yosida, *Theory of Magnetism*, (Springer, Berlin, 1996).

42. C. Tix, *Lower bound for the ground state energy of the no-pair Hamiltonian*, Phys. Lett. B **495**, 293-296 (1997).

43. X. Ren, P. Rinke, C. Joas and M. Scheffler, *Random-phase approximation and its applications in computational chemistry and materials science*, J. Mat. Sci. **47**, 7447-7471 (2012).

44. C.-O. Almbladh, U. von Barth, Z. D. Popovic, M. J. Stott, *Screening of a proton in an electron gas*, Phys. Rev. B 14, 2250-2254 (1976).

45. A. L. Fetter and J. D. Walecka, *Quantum Theory of Many-Particle Systems*, (McGraw-Hill, New York, 1971).

46. S. Raimes, *The wave mechanics of electrons in metals* (North-Holland Pub. Co., Amsterdam, 1963).

47. S. Raimes, *The theory of plasma oscillations in metals*, Rep. Prog. Phys. **20**, 1 (1957).

48. W. R. Johnson, C. D. Lin, K. T. Cheng, C. M. Lee, *Relativistic random-phase approximation*, Phys. Scr. **21**, 409 (1980).

49. S. T. Manson, *Relativistic-random-phase approximation calculations of atomic photoionization: what we have learned*, Canad. J.Phys. **87**, 5-8 (2009).

50. W. R. Johnson and K. T. Cheng, *Photoionization of the outer shells of neon, argon, krypton, and xenon using the relativistic random-phase approximation*, Phys. Rev. A **20**, 978 (1979).

51. W. R. Johnson, *Atomic Structure Theory* (Springer, New York, 2007).

52. P.C. Deshmukh, V. V. Radojevic, S. T. Manson. *Photoionization of the outer shells of radon and radium: Relativistic random-phase approximation for high-Z atoms*, Phys. Rev. A **45**, 6339-6348 (1992).

53. G. B. Pradhan, J. Jose, P. .C Deshmukh, L. A. LaJohn, R. H. Pratt and S. T. Manson, *Cooper minima: a window on nondipole photoionization at low energy*, J. Phys. B: At. Mol. Opt. Phys. 44, 201001 (2011).

54. A. F. Starace, *Atomic Photoionization*, in Handbuch der Physik, Vol. 3 (Springer, Berlin, 1983). pp. 1-121.

55. H. Shinohara, *Endohedral metallofullerenes*, Rep. Prog. Phys. **63**, 843 (2000).

56. T. Shoala, *Carbon nanostructures: detection, controlling plant diseases and mycotoxins*, in Micro and Nano Technologies (Elsevier, Amsterdam, 2020), pp. 261-277

57. R. T. Harding, S. Zhou, J. Zhou, T. Lindvall, W. K. Myers, A. Ardavan, G. A. D. Briggs, K. Porfyrakis and E. A. Laird, K. Porfyrakis, E. A. Laird, *Spin Resonance Clock Transition of the Endohedral Fullerene* $^{15}N@C_{60}$, Phys. Rev. Lett. **119**, 140801 (2017).

58. V. K. Dolmatov, *Confinement and electron correlation effects in photoionization of atoms in endohedral anions:* $Ne@C_{60}^{Z^-}$, J. Phys.: Conf. Ser. **212**, 012015 (2010).

59. P.C. Deshmukh, *Some recently found interchannel coupling effects in atomic photoionization processes*, Rad. Phys. Chemi. **70**, 515–523 (2004).

60. W. F. Luder, *Electron configuration as the basis of the periodic table*, J. Chem. Educ. **20**, 21 (1943).

61. B. Fricke, J. T. Waber, *Theoretical Predictions of the Chemistry of Superheavy Elements*, Northwestern University, Actinides Reviews **1**, 433-485 (1971).

62. R. H. Jonsson, *Information Transmission Without Energy Exchange*, Phys. Rev. Lett. **114**, 110505 (2015).

63. A. Müller1, S. Schippers1, J. Hellhund and A. L. D. Kilcoyne, *Photoionization of tungsten ions: experiment and theory for* W^{5+}, J. Phys. B: At. Mol. Opt. Phys. **52**, 195005 (2019).

64. S. Sahoo and Y. K. Ho, *On the Appearance of a Cooper Minimum in the Photoionization Cross Sections of the Plasma-Embedded Li Atom*, Res. Lett. Phys. 832413 (2009).

65. J. Jose, G. B. Pradhan, V. Radojević, S. T. Manson and P. C. Deshmukh, *Electron correlation effects near the photoionization threshold: the Ar isoelectronic sequence*, J. Phys. B: At. Mol. Opt. Phys. **44**, 195008 (2011).

66. S. T. Manson and J. W. Cooper, *Photo Ionization in the Soft X Ray Range: Angular Distributions of Photoelectrons and Interpretation in Terms of Subshell Structure*, Phys. Rev. **165**, 126 (1968).

67. U. Fano and J. W. Cooper, *Spectral Distribution of Atomic Oscillator Strengths*, Rev. Mod. Phys. **40**, 441 (1968).

68. A. Kivimäki, U. Hergenhahn, B. Kempgens, R. Hentges, M. N. Piancastelli, K. Maier, A. Ruedel, J. J. Tulkki A. M. and Bradshaw, *Near-threshold study of Xe 3d photoionization*, Phys. Rev. A **63**, 012716 (2000).

69. M. J. Puska and R. M. Nieminen, *Photoabsorption of atoms inside* C_{60}, Phys. Rev. A **47**, 1181 (1993).

70. J.-P. Connerade, V. K. Dolmatov and S. T. Manson, *On the Nature and Origin of Confinement Resonances,* J. Phys. B: At. Mol. Opt. Phys. **33**, 2279 (2000).

71. A. V. Korol and A. V. Solov'yov, *Confinement resonances in photoionization of endohedral atoms: myth or reality?*, J. Phys. B: At. Mol. Opt. Phys. **43**, 201004 (2010).

72. R. A. Phaneuf, A. L. D. Kilcoyne, N. B. Aryal, K. K. Baral, D. A. Esteves-Macaluso, C. M. Thomas, J. Hellhund, R. Lomsadze, T. W. Gorczyca, C. P. Ballance, S. T. Manson, M. F. Hasoglu, S. Schippers, and A. Müller, *Probing confinement resonances by photoionizing Xe inside a C^{+}_{60} molecular cage,* Phys. Rev. A **88**, 053402 (2013).